LA-UR-14-29495
Approved for public release; distribution is unlimited.

Title: Combined Molecular Simulation and Experimental Engineering of Organophosphorus Acid Anhydrase Yields Enhanced Neutralization of Organophosphorus Nerve Agents

Author(s): Phillips, Joshua Lee
Gnanakaran, Sandrasegaram
Harvey, Steven P.

Intended for: Nature Biotechnology

Issued: 2014-12-12

Combined Molecular Simulation and Experimental Engineering of Organophosphorus Acid Anhydrase Yields Enhanced Neutralization of Organophosphorus Nerve Agents

Joshua L. Phillips[1,2], Steven P. Harvey[3], and S. Gnanakaran[1]

[1]Theoretical Biology and Biophysics (T-6) and Center for Nonlinear Studies
Los Alamos National Laboratory, Los Alamos, NM 87545

[2]Department of Computer Science, Middle Tennessee State University,
Murfreesboro, TN 37132

[3]US Army Edgewood Chemical Biological Center, Aberdeen, MD 21010

Abstract

Organophosphorus nerve agents (ONAs) are highly toxic chemical species used in chemical warfare. The discovery of enzymes that catalyze the hydrolysis of ONAs have engaged significant research interest in understanding how these enzymes neutralize chemical warfare nerve agents. While Organophosphorus Acid Anhydrase (OPAA) has a mild capacity to neutralize V-type nerve agents, little work has focused on using simulation to predict activity enhancement/degradation for mutations in OPAA. We utilize molecular dynamics simulation to understand how mutations to OPAA enhance activity for the ONAs VX and VR found in experiment. We compare the performance of both non-bonded and bonded+electrostatics simulation models, and predict specific residues on OPAA amenable for future protein engineering studies. Our results indicate that bonded+electrostatics approaches are superior to non-bonded approaches at capturing interactions patterns consistent with experimental measurements, that differences in VX/VR head group structure account for enhanced hydrolysis of VR relative to VX, and identify specific residues as potentially good targets for future engineering studies.

Introduction and Background

Organophosphorus nerve agents (ONAs) are highly toxic chemical species used in chemical warfare.[1] Toxicity is caused by inactivation of the enzyme acetylcholinesterase (AChE) via phosphonylation of residue S200 within the enzyme's active site. AChE inhibition prohibits degradation and reuptake of the neurotransmitter acetylcholine within the synaptic cleft, leading to acute paralysis or death. The discovery of enzymes that catalyze the hydrolysis of ONAs have engaged significant research interest in understanding how these enzymes neutralize chemical warfare nerve agents[2-11] and how they might be employed for sanitation or therapeutic applications.[1, 12]

Two enzymes have been discovered which can effectively neutralize organophosphorus nerve agents by cleaving phosphate bonds in their respective target molecules (see Figure 1): phosphotriesterase (PTE) from *Pseudomonas diminuta*,[2-6] and organophosphorus acid anhydrase (OPAA) from *Alteromonas* sp. strain JD6.5.[7, 12] A wide variety of organophosphorus nerve agents have been synthesized for use as chemical weapons. Two key examples are GB (sarin) and VX. The remaining nerve agents share a large degree of structural and chemical similarity to either GB or VX, depending critically on the presence of a phosphofluoridate (P-F) or phosphonothioate (P-S) bond for G-type or V-type agents respectively (Figure 2). In addition, specific stereoisomers of these nerve agents show enhanced activity towards AChE compared to others, and nerve agent degrading enzymes also tend to show strong stereoselectivity towards these substrates. Activity enhancing mutations have been recently reported for PTE,[5, 8] and PTE simulation studies have provided additional insight on how mutations affect the dynamics of nerve agent binding.[10, 11, 13] However, little work has focused on using simulation to predict activity enhancement/degradation for mutations in OPAA.

Crystal structures show OPAA to be a 440 amino acid-long monomeric protein consisting of an amino domain and a carboxyl domain.[7] The latter exhibits a folded "pita-bread" pocket structure around the binuclear Mn^{2+} active site. Active site residues E244, E255, H336, D381, and D420 are bound to the Mn^{2+} ions, and an additional hydroxyl (OH-) group is bound to both ions in the absence of substrate. Co-crystal structures indicate that this hydroxyl group is displaced during binding with the inhibitor, mipafox (DDFP), or its hydrolysis product DDP. The last 77 residues could not be resolved in the available crystal structures, but deletion of this 77 AA-long tail resulted in no change in enzymatic activity, presumably indicating that the tail is completely disordered. An additional 15 residue-long (351-365) region was also observed to be disordered. However, this putatively disordered loop is in close proximity to the active site, and its role, if any, in substrate binding/hydrolysis has yet to be investigated. Additionally, Y212 and V342 were observed to interact with H343 to form a small pocket that binds to a DDP isopropyl group, indicating that mutations to these non-active site residues may be important for engineering enhanced activity towards OPAA substrates. Therefore, a primary goal of this work is to utilize molecular dynamics (MD) simulations of nerve agent

binding to the wild-type (WT) OPAA enzyme and a Y212F mutant in order to predict mutational efficacy for later experimental validation.

Our approach differs from the previous MD simulation work on ONA-degrading enzymes in two important ways. First, previous efforts have focused on utilizing non-bonded models for metalloprotein active sites.[10, 11, 13] Both PTE and OPAA are metalloproteins which coordinate a pair of metal ions in their active sites to perform nerve agent hydrolysis. The geometry of the metal center, which includes protein residues bound to the metal ions and one or more coordinated water molecules, must be maintained for efficient catalysis. The non-bonded (NB) models used in previous approaches remove all physical bonds between the metal ions and the surrounding residues and water molecules. Electrostatic partial charges and van der Waals interactions in standard MD forcefields are relied upon for maintaining the active site geometry. Furthermore, the constituent residues and ions in the active site are set to their formal atomic charge values which doesn't reflect how the partial atomic charges would need to be redistributed in the bonded network topology of the active site. We have sought to overcome such limitations by using a bonded+electrostatics (BE) model of the metal center.[14, 15] In this type of model, the active site geometry is maintained by explicitly including bonds between all active site residues, metal ions, and coordinated water molecules. MD potential parameters for the bonded atoms in the active site residues, and the partial atomic charges of the entire active site can be determined using quantum mechanical calculations. While BE models are more difficult to produce than NB models, BE models are becoming a common technique for modeling metal ion active sites in MD simulations.[14-16] Here, we simulate both NB and BE models of OPAA in order to compare the two methodologies. Second, these previous simulations have focused on the neutralization of G-type nerve agents, and not V-type agents. While WT OPAA shows only marginally detectable activity for V-type agents, our inhibition studies have shown that VX models as a competitive inhibitor of OPAA GD activity, consistent with binding of VX to the active site of OPAA. Protein engineering or evolution studies may facilitate enhanced activity, and would benefit from the insights gained from MD simulations of OPAA and V-type agent interactions. Previous studies have shown the P(-) isomer of the V-type agents to be far more toxic than the P(+) form, therefore we focus on the P(-) isomers of two V-type agents: VX and VR. Typically, chemical bonds are neither created nor removed in a classical MD simulation. Therefore, binding of substrates to the active site is considered sufficiently predictive of ONA hydrolysis, rather than observing a complete cycle from reactants to products. Even with this limitation, significant insights into the function of these enzymes can be obtained from classical MD.[10, 11]

Methods

Molecular Dynamics Simulations

Structures and simulation parameters for the VX and VR agents were prepared using standard protocols. First, structural models for VX and VR (P(-) isomers) were assembled using Chimera 1.6.2[17] and stored in MOL2 format. Next, we utilized the RED I.I.I.[18] software framework along with the Gaussian 09 quantum chemistry software package[19], to perform geometry optimization and calculate partial atomic

charges for these agents using the restrained electrostatic potential (RESP) technique. Next, the parmchk and tleap utilities of the AmberTools[20] package were used to compile the bonded parameters for the agents using the Generalized AMBER Forcefield (GAFF).[21]

The crystal structure of OPAA (PDB:3L7G) was used to prepare a suitable structure for simulation.[7] The WT amino acid sequence of OPAA is 517 AAs in length, but the crystal structure is lacking the 77 AA-long C-terminus due to presumed disorder. Since this region has no known effect on OPAA function, it was not considered in our simulations. Of the remaining 440 AAs, the crystal structure is also lacking a 15 AA-long portion of the sequence (AAs 351-365), again presumed to be disordered. Since this short loop region is relatively close to the active site of the OPAA enzyme, we used Modeller 9.10[22] to construct a PDB file of WT OPAA which included the missing loop region; the 3L7G crystal structure served as the model template. The Y212F mutant was prepared in Pymol[23] based on the WT OPAA model using the mutagenesis wizard. The two Mn ions bound to the active site residues of OPAA were placed in the OPAA models according to their locations in the crystal structure. Analogous atoms for the inhibitor, mipafox, which is bound to the active site in the OPAA crystal structure, were determined for both VX and VR. The VX and VR structures were then oriented to minimized the RMSD between analogous atoms in the inhibitor and nerve agents using VMD 1.9.1[24], producing a putatively VX- or VR-bound model for both WT and Y212F OPAA.

For the non-bonded (NB) model, simulation parameters for all protein residues were taken from the Amber ff99SB-ILDN forcefield.[25] The Mn ions were each given a +2 integer charge, and non-bonded (Lennard-Jones) parameters for these ions were taken from the study by Bradbrook et al.[26] In this model, any bonds between the Mn ions and the active site residues reported in the crystal structure were ignored.

In the bonded+electrostatics (BE) model, protein residues were parameterized using the Amber ff99SB-ILDN forcefield[25], except for those bonded directly to the Mn ions in the crystal structure. For these residues, additional bonds to the Mn ions were parameterized using the Metallo-Center Protein Builder (MCPB)[14] tool included in the AmberTools[20] package according the standard protocol outlined in the AmberTools documentation. The MCPB utilizes Gaussian 09[19] to perform geometry optimization of the active site residues and Mn ions. The optimized structure is used to calculate new partial charges for all atoms in the active site using the RESP technique with backbone charges restrained as in other Amber forcefields.[27] It was necessary to give the active site an overall formal charge of +1 since the remaining crystal structure (PDB ID: 3L24) published by Vyas et al. shows a single hydroxyl group bound to the active site (absent of inhibitors/substrates) and this hydroxyl group is displaced by the inhibitor, mipafox, in the 3L7G crystal structure. [7] Additionally, MCPB utilizes a frequency analysis of the optimized structure to extract bonded parameters (including bond lengths, angles, and torsional angles) for all bonds between the Mn ions and surrounding atoms. All remaining parameters for the active site residues are taken from the GAFF[21], and the non-bonded parameters for Mn were again taken from Bradbrook et al.[26]

AMBER parameter/topology files for the NB model, BE model, VX and VR were created using the tleap program in AmberTools using the respective parameter sets described above, and these files were then converted into GROMACS[28] format using the amb2gmx.pl script.[29] Finally, the VX and VR structures were placed into the initial, bound configurations (as described above) for the WT and Y212F mutants and for both models to create a total of eight simulation conditions: VX-WT-NB, VR-WT-NB, VX-Y212F-NB, VR-Y212F-NB, VX-WT-BE, VR-WT-BE, VX-Y212F-BE, and VR-Y212F-BE. These structures were then centered in a $10nm^3$ box, and solvated using TIP3P water, 0.15 molar NaCl, and minimized using 100000 steps of steepest descents. The minimized structures were then run for 500ps of molecular dynamics as an NPT ensemble with position restraints on the heavy atoms of the protein. Pressure was maintained at 1 bar using the isotropic Parrinello-Rahman method[30] (τ_p=1). Initial random velocities were chosen from the Maxwell-Boltzmann distribution at 300K, and temperature was maintained using Bussi's velocity rescaling thermostat[31] (τ_t=0.1) coupled separately to the solvent and the protein. All hydrogen bonds were constrained using the LINCS algorithm[32, 33], allowing for a 2fs time-step. Long-range electrostatics were treated using the smooth PME method[34] with a 1.4Å cut-off, and a shifted cut-off (0.9-1.2 Å) potential was used for van der Waals interactions. After these initial equilibration simulations, each of the conditions were replicated 5 times as an NVT ensemble at 300K without position restraints for 50ns after reinitializing the atomic velocities. Snapshots from the 50ns simulations were captured every 20ps (2500 frames per simulation, 12500 frames per condition, and 100000 frames in total for all simulations). All of these simulations were performed using GROMACS 4.5.6[28, 35-37] and the aggregate simulation time for the entire study was 2μs (8 structures * 5 replicates * 50ns).

Simulation Analysis

Quantification of the interactions between the protein and the V-type agents was performed by constructing contact profiles. A contact profile consists of a set of probabilities which indicate how often the atoms in nerve agents are in close proximity to heavy atoms in the protein. The contact profile is constructed by taking each frame from the simulation trajectories and calculating the distances between each atom in the nerve agent and each heavy atom in the protein. Any pair of atoms found to be within a distance of 5Å were considered to be in contact. The probability of contact for any pair of atoms was then calculated by taking the number of contacts found and dividing it by the total number of frames making the probability of contact between these atoms simply the fraction of all frames where this contact was present. Likewise, the contact probabilities between the Mn ions and the V-type agent atoms were included in the analysis as well. Therefore a complete contact profile consists of an N by M matrix of contact probabilities where N is the number of atoms in the V-agent and M is the number of heavy atoms in the protein plus the two metal ions. A contact profile was constructed for all eight simulation conditions listed in the previous section.

The majority of entries in the contact profile matrices are zero, and many others show such low contact probability that they are effectively zero. In order to discern differences between contact profiles, only heavy atoms having at least one contact

probability above P_{cutoff} are included in all plots shown, where $P_{cutoff} = 0.1$. The value of P_{cutoff} was chosen by plotting the *mean contact probability* (and standard error) for each heavy atom and selecting a value for P_{cutoff} that captured the visible variations among the profiles. The plots for each of the eight conditions are shown in Supplemental Figures 1-4. VMD was used to visualize these contact probabilities on the OPAA structure by coloring the heavy atoms meeting the P_{cutoff} criterion appropriately. These colored structures are shown in Figures 4-11. Since there is no automated way to select such a cutoff, it is possible that too large a cutoff will result in loss of important features for comparing the profiles. We have included plots for $P_{cutoff} = 0.01$ in Supplemental Figures 10-11 showing that no additional features are revealed when using a small cutoff.

While the mean contact probability plots reveal important protein heavy atom contacts for the nerve agents, they do not show which parts of the nerve agent molecules are in contact with these atoms. Therefore, heatmaps were also generated for heavy atoms having at least one contact probability above P_{cutoff}, and these are shown in Supplemental Figures 1-4. The ordering of the atoms along the y-axis in the heatmaps roughly correspond to the 3D structure of the nerve agents with atoms near the “head” of the molecules on one end of the y-axis and atoms near the “tail” of the molecules on the other end of the y-axis. This layout allows for orientation preferences of the nerve agents to be determined from these plots, in addition to overall contact probability.

Finally, to compare two different simulation conditions the contact profile from one condition was subtracted from another. Mean differences (and standard error) in contact probability for each heavy atom meeting the earlier $P_{cutoff} = 0.1$ criterion were plotted using these data. Also, VMD was used to visualize these differences on the OPAA structure using a divergent color map (blue-white-red), and this color map was used to generate mean difference heatmaps as well. These plots facilitate more accurate visual and quantitative comparison between the various simulation conditions. All three difference plots were constructed to compare the non-bonded model to the bonded+electrostatics model (Supplemental Figures 6-7), WT protein to the Y212F mutant (Supplemental Figure 8), and VX to VR (Supplemental Figure 9). Contact profile difference plots for $P_{cutoff} = 0.01$ are shown in Supplemental Figures 12-14.

Results and Discussion

Comparison of the Non-bonded Model and the Bonded+Electrostatics Model

We analyzed the contact profile data to assess whether the NB or BE model more accurately captures the trend in the experimental results which showed an increase activity toward both VX and (even more so) VR for the Y212F mutant compared to WT OPAA. First, we compared the preferred contacts between the two models for VX and WT OPAA (VX-WT-NB and VX-WT-BE). As shown in Figure 4, VX prefers to associate with residues directly beside the active site in the NB model, primarily H332 and H336, but also with H363 which is located in the short disordered loop. Less frequent preferences were observed for G335, H343 and E381 in the NB model as well, again in the same pocket beside the active site. The BE model on the other

hand, indicated that VX prefers to associate in two distinct locations: closer to the active site as shown by increased contact with Y212, or on the periphery of the active site near residues Y292 and F378 near the base of the disordered loop. These patterns are clearly distinct with the NB model showing a strong binding of VX directly beside the active site, and the BE model showing that VX moves back and forth between the active site and the base of the disordered loop. In order to assess the ability of the models to match the experimental data, we then compared the preferred contacts for VR (VR-WT-NB and VR-WT-BE) since activity towards VR is slightly higher than VX in WT OPAA. Figure 5 indicates that VR prefers to occupy a similar location in the NB model as VX, focusing on residues H332, H336, and E381 with some additional contact with disordered loop residue H365. However, the BE model showed fewer contacts with the residues at the base of the disordered loop. Instead, VR seems to be more focused around Y212, G213, and I215.

The above results indicate that the NB model cannot effectively explain why WT OPAA shows increased activity toward VR since the contact patterns for VX and VR are quantitatively and qualitatively too similar. However, the BE model results indicate that this model is capable of distinguishing between these two, highly similar compounds. This is shown by the decreased contact between VR and the residues at the base of the disordered loop as compared to VX, allowing VR to spend more time interacting directly with the active site in a manner more consistent with the experimental results.

An even stronger disparity between the NB and BE models can be found in the interactions between VX or VR and the Y212F mutant. In Figure 6, VX is reoriented around the binding pocket in the NB model, still showing strong contacts with residues H332, H336 and E381 as in the WT, but now having the tail of the molecule favoring interactions with L225, R418, and Y385. The BE model shows a preference for interacting with F212 and H343, similar to VR in the WT above. Figure 7 shows VR interacting with similar residues as VX in the NB model. In particular, the tail of the ligand interacts with H332, L225, R418, and Y385. However, the BE model shows a striking distinction from previous simulations where contacts are increased for D255, D244, F212, I215, and V342. Additionally, VR contacts with the Mn ions are considerably higher in the BE model compared to the NB model.

Overall, the NB model showed little difference between the contact patterns of VX and VR with the Y212F mutant (see Supplemental Figure 12). However, the BE model showed that VX moved into the active site in the mutant to a similar location as VR in the WT above. Additionally, VR showed enhanced contact with residues F212, I215, V342 and the Mn ions, suggestive of strong binding directly to the active site. Hence, the NB model shows little dynamic range in terms of distinguishing between the different ligands for the Y212F mutant, and is also inconsistent with the experimental results. Primarily, the NB simulations indicate that differences between VR and VX were greater in the WT compared to the Y212F mutant, and the opposite was shown to be true in experiment. Finally, the BE model shows distinct contact patterns between VX and VR in the WT which suggests slightly enhanced binding of VR, and the contact patterns in the Y212F mutant suggest enhanced binding of VX compared to WT, but even more striking enhancement of VR binding.

These results suggest that BE models are preferred to NB models for both making critical distinctions between compounds/mutations and matching experimental trends.

Comparison of WT OPAA and the Y212F Mutant

We analyzed contact profile data from the BE simulations of VX or VR interacting with WT OPAA and the Y212F mutant to determine what specific residues are involved in these interactions, and to help understand why the Y212F mutant shows greater activity for the V-agents. Figure 8 shows a direct comparison between the contact profiles for VX with WT OPAA and the Y212F mutant (VX-WT-BE and VX-Y212F-BE). Contacts at the base of the disordered loop are prevalent in the WT, but the Y212F mutant shows more contact with H336, E381, and the metal ions. However, the distinction is not perfect since there was slightly more contact with Y212 and V342 in the WT, and the Y212F mutant shows additional contacts with residues more distant from the active site (H154 and N145). However, the Y212F mutant also shows additional interactions with H356 and P360 which are part of the disordered loop, indicating that the head of VX is often oriented to point away from the active site while the tail binds with H336 and E381. The interactions of VX with the WT at residues Y212 and V342 were not much greater than the Y212F mutant, indicating that the WT places VX near the base of the disordered loop instead of near the active site and that VX only transiently enters the active site. However, the Y212F mutant consistently places the tail of the VX molecule in the active site, with the head interacting with H356 or P360. Therefore, the mechanism used by the Y212F mutant to consistently keep VX nearer to the active site than the WT must be via the active site interactions with the tail of VX, making transient binding of the head with the opposite side of the active site more likely on average.

The results for VR (VR-WT-BE and VR-Y212F-BE) are clearer, and indicate a similar mechanism for enhanced function in the Y212F mutant. Figure 9 shows how the WT prefers to place VR close to the base of the disordered loop (H296 and H300), but the Y212F mutant places VR directly over the active site. The H336 and E381 sites show more contacts with the tail of VR, as well as the Mn ions. Additionally, there are significantly more contacts with D255 and D244 (both bound to the Mn ions) and the surrounding pocket (V342, F212, and I215). Again, the head of the ligand is placed into this pocket, and the resulting orientation is putatively responsible for the enhanced activity. The P-S bond of VR is placed relatively close to the Mn ions in this configuration compared to the WT or VX simulations. It appears that the head of VR is too bulky to allow it to slide deeper into the active site and place this bond directly over the ions, or allow the phosphoryl oxygen to bind between the two ions. However, these data suggest that the mechanism of enhanced activity for the Y212F mutant is both closer proximity and improved relative orientation of the P-S bond compared to the WT. It is unclear exactly why changing the slightly polar sidechain of tyrosine to the non-polar sidechain of phenylalanine at site 212 would give rise to this effect, but we suggest that removal of the hydroxyl group makes it easier for the ligand to exchange positions with water molecules in the active site. Regardless, the Y212F mutant allows the head of VX and VR (even more so) to bind more effectively opposite the tail across the active site.

The NB model did not match the experimental trends as well as the BE model (see Supplemental Figure 13), and the data from the NB simulations did not suggest a clear mechanism for enhancement. For WT OPAA, the interactions were mainly with H363 for VX and with several different histidines surrounding the active site (H296, H300, H363, H365, and H336) for VR. In this case, the data is consistent with experiment in that VR is more mobile than VX. Therefore, VR putatively binds to the active site more often than VX via transient interactions. However, this is not the case for the Y212F mutant. Both VX and VR showed higher contacts between the tail and residues H332 and Y385 for the Y212F mutant. These contacts are far too distant from the active site to suggest enhanced function. To be fair, the VR data shows slightly more contacts with F212, D244, and I215 in the mutant compared to the WT and similar to the BE simulations, but the head more often interacts strongly with N418 and L225 overall. This was also the case for VX and suggests that both VX and VR spend more time bound to H332, Y385, N418, and L225. The transient interaction hypothesis mentioned above cannot explain these results since the more prevalent contacts for the Y212F mutant are not in the active site. Again, the limited dynamic range of the NB results prohibits making a clear distinction between the WT and the Y212F mutant, and it is not clear which interactions near the active site are responsible for the enhanced activity.

Comparison of VX and VR

We analyzed the contact profile data from the BE simulations to ascertain why the structure of VR is preferred over VX as evidenced by enhanced binding in the experiments. First, we compared data from the WT OPAA simulations of VX and VR (VX-WT-BE and VR-WT-BE) to assess what residues prefer VX or VR. Figure 10 shows that the head of VR, which has a slightly bulkier head than VX due the presence of two extra methyl groups, fits into the binding pocket near Y212 better than VX. In contrast, the head of VX is often disengaged from the active site when the tail is interacting with histidine residues in the disordered loop (H363 or H343). Therefore, while the tail of VR is more promiscuous in interacting with more distant histidines (H296 or H300) a significant fraction of the time, the head of VR is capable of binding more stably to the Y212 pocket without falling off due to tail interactions with the disordered loop histidines. For the Y212F simulations, both VX and VR interact less with the histidines in the disordered loop, presumably due to enhanced binding to the F212 pocket (see Figure 11). However, VR shows significantly more contacts with the pocket than VX, suggesting that combining bulkier head groups with the more favorable F212 mutation is the cause for the preferential VR enhancement. This is consistent with the earlier comparisons between WT OPAA and the Y212F mutant, where specific contacts for F212 pocket residues were observed. The Y212F mutation still had a noticeable effect on VX interactions as well, even though VX did not remain in the F212 pocket. Earlier discussions comparing the WT OPAA and Y212F mutant simulations of VX confirm this by showing that the WT enzyme orients the tail toward the disordered loop while the Y212F mutant orients the tail to the active site at residues H336, E381, and toward the metal ions. While the head still fails to bind effectively for VX, our results suggest that the reorientation of the molecule in the Y212F mutant is responsible for the increased activity for VX observed in the experiments.

The NB model results (see Supplemental Figure 14) show little difference between VR and VX for the WT simulations. Generally, VX and VR both interact with active site residues with nearly equivalent probability (only slightly higher for VR). Instead, primarily the patterns of histidine interactions are different between the two ligands as described in the previous section. On the other hand, the Y212F simulations indicate that VX contacts the F212 pocket slightly less than VR, but the dynamic range is limited (~5% differences) compared to the differences observed in the BE model (~30%) and the most significant contacts observed were outside of the active site (e.g. F365).

Role of the 15AA Disordered Loop

Persistent interactions with the disordered loop (particularly the loop histidine residues H343 or H363) often occur in either model, but much more so in the NB model (see Figures 4-7). Given that the BE model allows for more favorable contact with the Y212 pocket, it may be that substrates are simply less accessible to loop residues in these simulations. Similarly, the NB model rarely showed significant binding in the Y212 pocket, and this may be the cause of the overrepresentation of contacts in the loop region. Nevertheless, the BE model still shows significant contacts for loop residues in WT OPAA as described in the previous sections. Therefore, it is difficult to assess whether these interactions are propitious or deleterious. Our results for VX suggest that these interactions might be deleterious by destabilizing binding of the small head group of VX to the Y212 pocket. However, our VR results suggest that these interactions become almost negligible once strong binding to the pocket is established. In addition, the loop may perform “flycasting”[38-40] in order to pull in new substrate or clear the active site of products following catalysis. Regardless, we observe some interactions between the substrates and the disordered loop, suggesting that modifying this region would impact activity in some manner.

Predicting Activity Enhancing Mutations

We utilized the results and analyses above to predict specific residues which might be good targets for future engineering studies. Since most of the data for the NB model could not definitively show a difference in many of the cases above, we again focus on the results of the BE model. Overall, there are two possible strategies that we can develop using our simulations to predict potential sites for mutagenesis. The first strategy involves suggesting sites which stabilize the bound configuration. We used the contact profile differences between WT OPAA and the Y212F mutant or VX and VR to guide these suggestions. In particular, comparing the VR-Y212F-BE model to other simulations as shown in the previous sections indicated that stabilization of interactions in the F212 pocket should facilitate catalysis. There were two residues in direct proximity of F212 which were often in contact with VR: G213, N214, I215 and V342. Mutation of G213 may result in the inability of F212 to allow room for the substrate to enter the pocket and N214 appears to form tertiary interactions that stabilize the fold of the protein. So these two sites may not be the best targets. However, the strongest contacts were for I215 and V342, and there are no structural considerations prohibiting these sites. Interestingly, V342 was also mentioned by Vyas et al. as forming part of a binding pocket for one of the isopropyl groups of

mipafox.[7] Mutations to these sites which stabilize interactions with VX, VR, or both should result in stronger binding to the active site and enhanced activity. The second strategy involves suggesting sites which interfere with entry to the active site. Mutations which reduce substrate affinity to these sites may indirectly enhance binding to the active site, essentially eliminating competition for binding. The majority of contacts outside of the active site were found in histidine residues across all simulations in this study, suggesting that mutating the histidines may result in less competition for substrate with the active site. H343 and H363 in the disordered loop both showed significant interactions VR and VX, suggesting that these may be good targets. However, the VR-WT-BE model also favored H332, H296, and H300. However, this approach is inherently a double-edged sword since these interactions may play an important role in enhancing the local concentration of substrate near the active site, or perform “flycasting” as mentioned in the previous section. Therefore, it is not clear that mutations at these sites will be propitious or deleterious, but they play an important role in substrate interactions nonetheless.

Given that the Y212F mutant shows more activity for VR over VX and that the BE model seems to provide a better insights into this effect, a natural result of this study would be to identify differences between the contact profiles of VR and VX in the BE model in order to determine possible sites for future mutation studies, and potential activity enhancement. Some residues enhanced for VR over VX, such as D244 and D255, coordinate the Mn ions and may not be amenable to mutation. Additional residues in the proximity of F212 were enhanced for VR: G213, N214, I215, and V342. Mutating G213 may disrupt the orientation of the F212 sidechain, and the N214 sidechain is not facing toward the binding pocket. This leaves I215 and V242 as possible targets, since they both orient toward the binding pocket. Interestingly, V342 is mentioned in Vyas et al. along with Y212 for creating a binding pocket for one of the isopropyl groups of mipafox. Finally, while interactions with the disordered loop were reduced in the BE model, the loop may still participate in flycasting effects where substrate is captured in the bulk or product is captured from the active site. Interactions with H363 were prevalent in many simulations, suggesting that mutations to this site could be useful to determine the role of the loop.

Conclusion

The enzyme OPAA has a mild capacity to neutralize V-type nerve agents, and engineered mutants with enhanced activity would be useful for therapeutic or sanitation purposes. Recent experimental work has shown that the Y212F mutant shows enhanced activity for VX and (even more so) for VR. We have utilized NB and BE molecular dynamics simulations to study both WT OPAA and the Y212F mutant in the presence of the substrates VX and VR. The BE model showed close agreement with experimental results, indicating enhanced activity for VX and VR in the Y212F mutant. While the NB model showed a trend for higher VR activity than VX in WT OPAA, it was unable to clearly distinguish between VR and VX for the Y212F mutant, suggesting that the BE modelling approach is superior to the NB approach. The simulations showed that the tail of the VX and VR molecules interact primarily with residues H336 and E381 of the active site, but also show affinity for residues H343

and H363 in the disordered loop, or with H296, H300, and H332 outside of the active site. Importantly, the BE model simulations revealed that the Y212F mutant enhanced binding via interactions with the head groups of VR, and that surrounding residues I215 and V342 also participate in forming a binding pocket which stabilizes VR within the active site. The head of VX lacks two additional methyl groupsfound in VR, contributing to less favorable interactions with the F212 pocket and thus less stable binding overall. Mutagenesis of residues I215 or V342 (in conjunction with Y212F) may result in more stable head group binding and enhanced activity for VX, VR, or both. Additionally, mutagenesis of target histidine residues outside of the active site may decrease competition for substrate binding and enhance activity. However, these resides may instead be responsible for increasing the local concentration of substrate via flycasting or even aid the removal of product after catalysis. Future work will focus on the effects of mutations to these histidine residues in order to more precisely predict which effect is the dominant mechanism.

References

1. Kim, K., Tsay, O.G., Atwood, D.a. & Churchill, D.G. Destruction and detection of chemical warfare agents. *Chemical Reviews* **111**, 5345-5403 (2011).
2. Benning, M.M., Hong, S.B., Raushel, F.M. & Holden, H.M. The binding of substrate analogs to phosphotriesterase. *Journal of Biological Chemistry* **275**, 30556-30560 (2000).
3. Benning, M.M., Shim, H., Raushel, F.M. & Holden, H.M. High resolution X-ray structures of different metal-substituted forms of phosphotriesterase from Pseudomonas diminuta. *Biochemistry* **40**, 2712-2722 (2001).
4. Benning, M.M., Kuo, J.M., Raushel, F.M. & Holden, H.M. Three-dimensional structure of the binuclear metal center of phosphotriesterase. *Biochemistry* **34**, 7973-7978 (1995).
5. Hill, C.M., Li, W.-S., Thoden, J.B., Holden, H.M. & Raushel, F.M. Enhanced degradation of chemical warfare agents through molecular engineering of the phosphotriesterase active site. *Journal of the American Chemical Society* **125**, 8990-8991 (2003).
6. Grimsley, J.K., Calamini, B., Wild, J.R. & Mesecar, A.D. Structural and mutational studies of organophosphorus hydrolase reveal a cryptic and functional allosteric-binding site. *Archives of Biochemistry and Biophysics* **442**, 169-179 (2005).
7. Vyas, N.K., Nickitenko, A., Rastogi, V.K., Shah, S.S. & Quiocho, F.A. Structural insights into the dual activities of the nerve agent degrading organophosphate anhydrolase/prolidase. *Biochemistry* **49**, 547-559 (2010).
8. Bigley, A.N., Xu, C., Henderson, T.J., Harvey, S.P. & Raushel, F.M. Enzymatic neutralization of the chemical warfare agent VX: evolution of phosphotriesterase for phosphorothiolate hydrolysis. *Journal of the American Chemical Society* **135**, 10426-10432 (2013).
9. diSioudi, B., Grimsley, J.K., Lai, K. & Wild, J.R. Modification of near active site residues in organophosphorus hydrolase reduces metal stoichiometry and alters substrate specificity. *Biochemistry* **38**, 2866-2872 (1999).

10. Gomes, D.E.B., Lins, R.D., Pascutti, P.G., Straatsma, T.P. & Soares, T.A. Molecular Models to Emulate Confinement Effects on the Internal Dynamics of Organophosphorous Hydrolase. *LINCS: Advances in Bioinformatics and Computational Biology* **5167**, 68-78 (2008).
11. Soares, T.A., Osman, M.A. & Straatsma, T.P. Molecular Dynamics of Organophosphorous Hydrolases Bound to the Nerve Agent Soman. *Journal of Chemical Theory and Computation* **3**, 1569-1579 (2007).
12. DeFrank, J.J. et al. Screening of halophilic bacteria and Alteromonas species for organophosphorus hydrolyzing enzyme activity. *Chemico-biological Interactions* **87**, 141-148 (1993).
13. Fairchild, S.Z. et al. Computational characterization of how the VX nerve agent binds human serum paraoxonase 1. *Journal of Molecular Modeling* **17**, 97-109 (2011).
14. Peters, M.B. et al. Structural Survey of Zinc Containing Proteins and the Development of the Zinc AMBER Force Field (ZAFF). *Journal of Chemical Theory and Computation* **6**, 2935-2947 (2010).
15. Hoops, S.C., Anderson, K.W. & Merz, K.M. Force field design for metalloproteins. *Journal of the American Chemical Society* **113**, 8262-8270 (1991).
16. Sindhikara, D.J., Roitberg, A.E. & Merz, K.M. Apo and nickel-bound forms of the Pyrococcus horikoshii species of the metalloregulatory protein: NikR characterized by molecular dynamics simulations. *Biochemistry* **48**, 12024-12033 (2009).
17. Pettersen, E.F. et al. UCSF Chimera--a visualization system for exploratory research and analysis. *Journal of Computational Chemistry* **25**, 1605-1612 (2004).
18. Dupradeau, F.-Y. et al. The R.E.D. tools: advances in RESP and ESP charge derivation and force field library building. *Physical Chemistry Chemical Physics* **12**, 7821-7839 (2010).
19. Frisch, M.J. et al. Gaussian 09 Revision D.01.
20. Case, D.A. et al. AMBER 12, Vol. 85. (University of California, San Francisco; 2012).
21. Wang, J., Wolf, R.M., Caldwell, J.W., Kollman, P.A. & Case, D.A. Development and testing of a general amber force field. *Journal of Computational Chemistry* **25**, 1157-1174 (2004).
22. Eswar, N. et al. in Current Protocols in Protein Science, Vol. Chapter 2 Unit 2.9 (2007).
23. Schrodinger, L. The PyMOL Molecular Graphics System, Version 1.4.1. (2010).
24. Humphrey, W., Dalke, A. & Schulten, K. VMD: visual molecular dynamics. *Journal of Molecular Graphics* **14**, 33-38, 27-38 (1996).
25. Lindorff-Larsen, K. et al. Improved side-chain torsion potentials for the Amber ff99SB protein force field. *Proteins: Structure, Function, and Bioinformatics* **78**, 1950-1958 (2010).
26. Bradbrook, G.M. et al. X-Ray and molecular dynamics studies of concanavalin-A glucoside and mannoside complexes Relating structure to thermodynamics of binding. *Journal of the Chemical Society, Faraday Transactions* **94**, 1603-1611 (1998).

27. Wang, J., Cieplak, P. & Kollman, P.A. How well does a restrained electrostatic potential (RESP) model perform in calculating conformational energies of organic and biological molecules? *Journal of Computational Chemistry* **21**, 1049-1074 (2000).
28. Hess, B., Kutzner, C., van der Spoel, D. & Lindahl, E. GROMACS 4: algorithms for highly efficient, load-balanced, and scalable molecular simulation. *Journal of Chemical Theory and Computation* **4**, 435-447 (2008).
29. Mobley, D.L., Chodera, J.D. & Dill, K.a. On the use of orientational restraints and symmetry corrections in alchemical free energy calculations. *Journal of Chemical Physics* **125**, 084902 (2006).
30. Parrinello, M. & Rahman, A. Polymorphic transitions in single crystals: A new molecular dynamics method. *Journal of Applied Physics* **52**, 7182 (1981).
31. Bussi, G., Donadio, D. & Parrinello, M. Canonical sampling through velocity rescaling. *Journal of Chemical Physics* **126**, 014101 (2007).
32. Miyamoto, S. & Kollman, P.a. Settle: An analytical version of the SHAKE and RATTLE algorithm for rigid water models. *Journal of Computational Chemistry* **13**, 952-962 (1992).
33. Hess, B. P-LINCS: A Parallel Linear Constraint Solver for Molecular Simulation. *Journal of Chemical Theory and Computation* **4**, 116-122 (2008).
34. Essmann, U. et al. A smooth particle mesh Ewald method. *Journal of Chemical Physics* **103**, 8577 (1995).
35. Berendsen, H.J.C., van der Spoel, D. & van Drunen, R. GROMACS: A message-passing parallel molecular dynamics implementation. *Computer Physics Communications* **91**, 43-56 (1995).
36. Lindahl, E. & Hess, B. GROMACS 3 . 0 : a package for molecular simulation and trajectory analysis. *Journal of Molecular Modeling*, 306-317 (2001).
37. Van Der Spoel, D. et al. GROMACS: fast, flexible, and free. *Journal of Computational Chemistry* **26**, 1701-1718 (2005).
38. Shoemaker, B.A., Portman, J.J. & Wolynes, P.G. Speeding molecular recognition by using the folding funnel: the fly-casting mechanism. *Proceedings of the National Academy of Sciences* **97**, 8868-8873 (2000).
39. Sugase, K., Dyson, H.J. & Wright, P.E. Mechanism of coupled folding and binding of an intrinsically disordered protein. *Nature* **447**, 1021-1025 (2007).
40. Huang, Y. & Liu, Z. Kinetic Advantage of Intrinsically Disordered Proteins in Coupled Folding-Binding Process: A Critical Assessment of the "Fly-Casting" Mechanism. *Journal of Molecular Biology* **393**, 1143-1159 (2009).

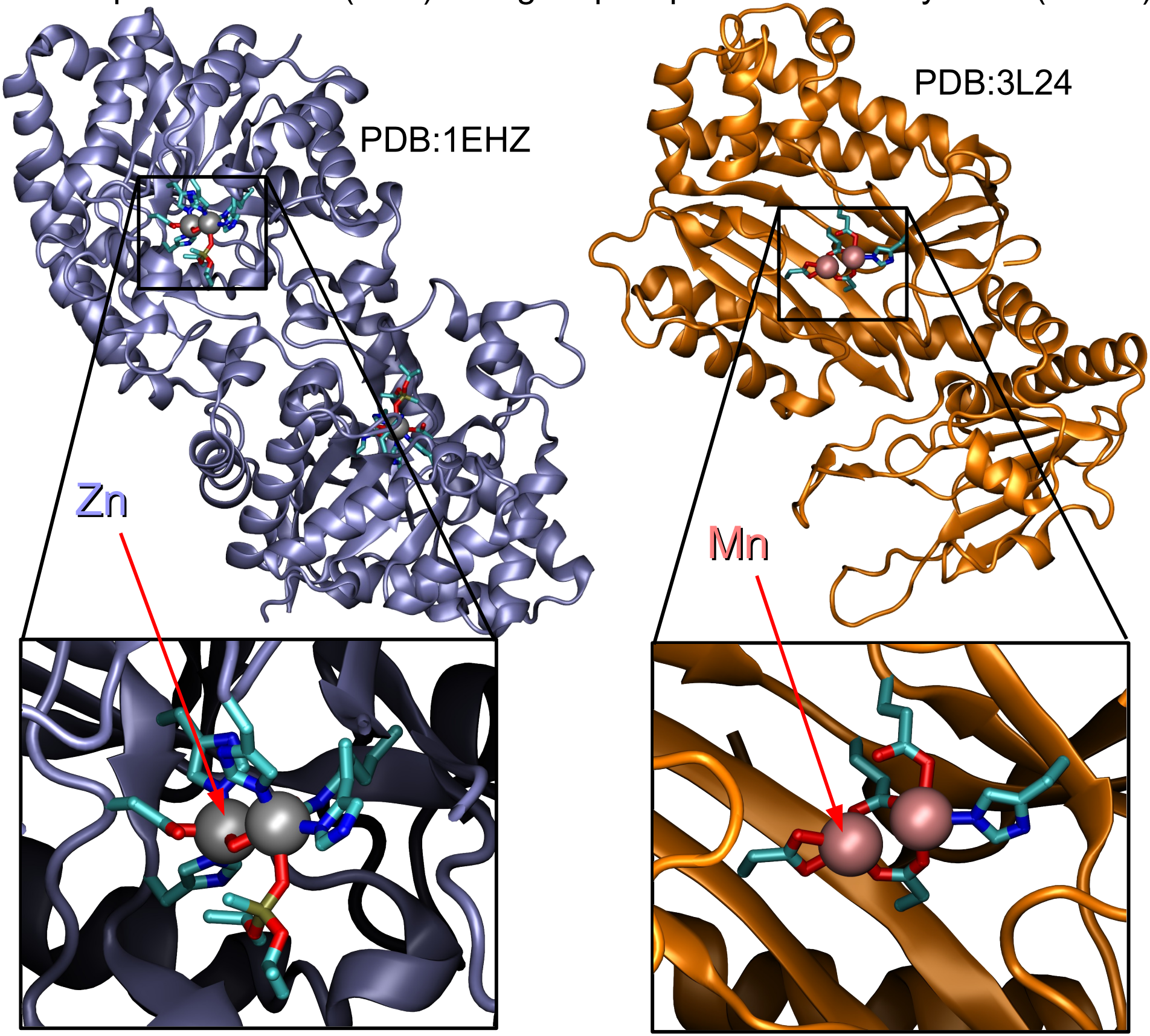
Phosphotriesterase (PTE)
Organophosphorus Acid Anhydrase (OPAA)
PDB:1EHZ
PDB:3L24
Zn
Mn

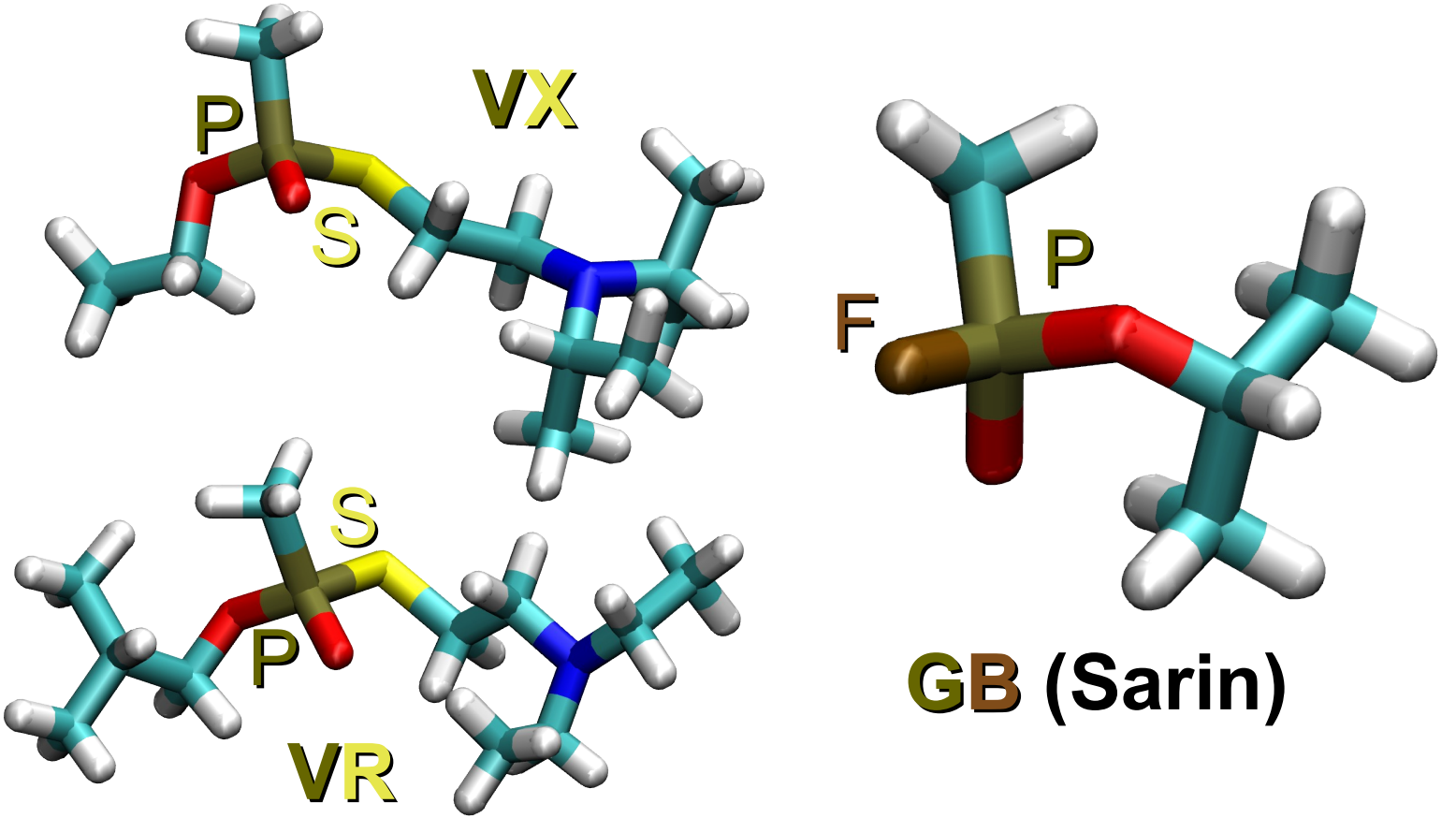
VX
P
S
S
P
VR
F
P
GB (Sarin)

Contact mapping procedure for WT OPAA interactions with VX P(-) [VX-WT-NB]

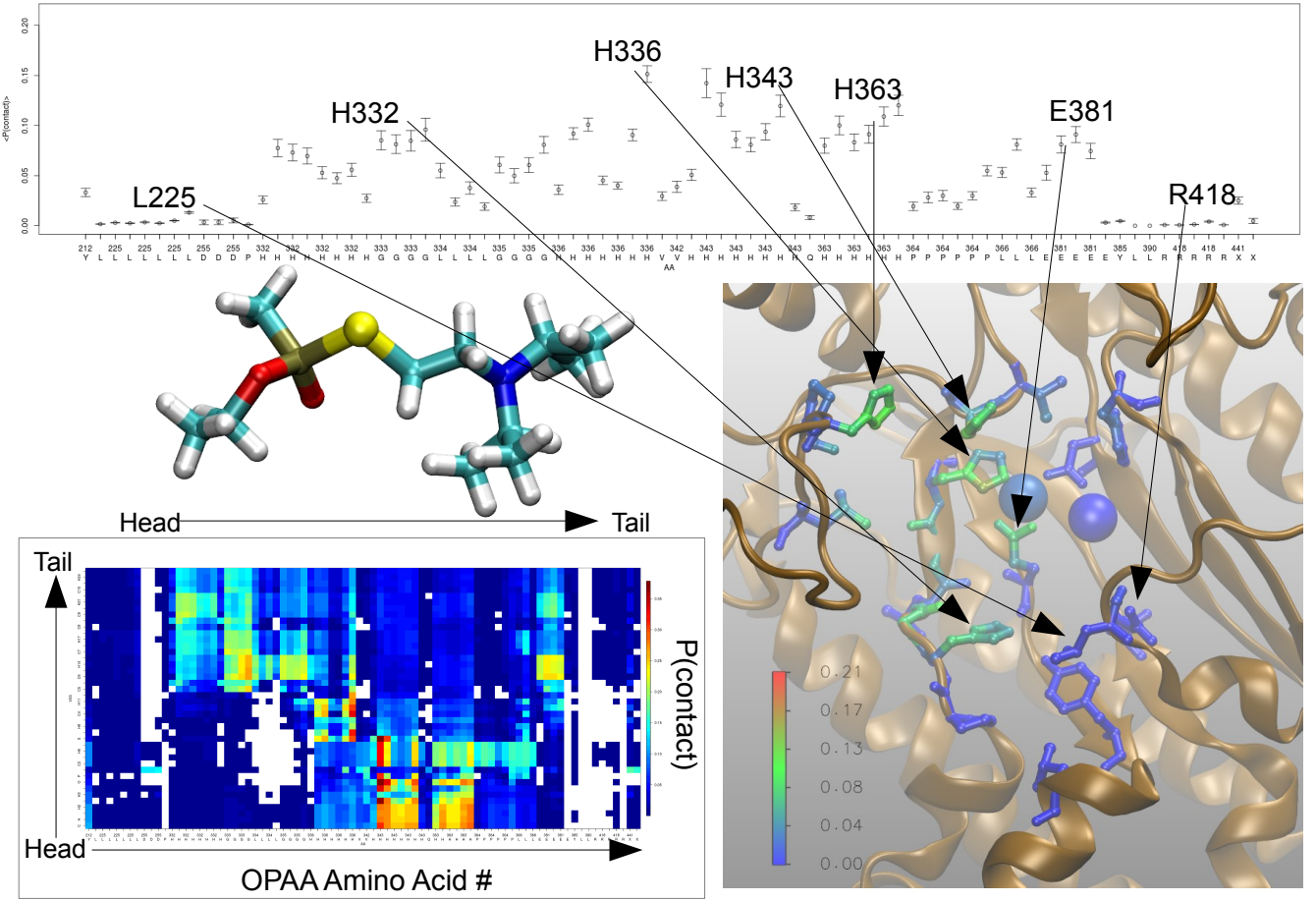

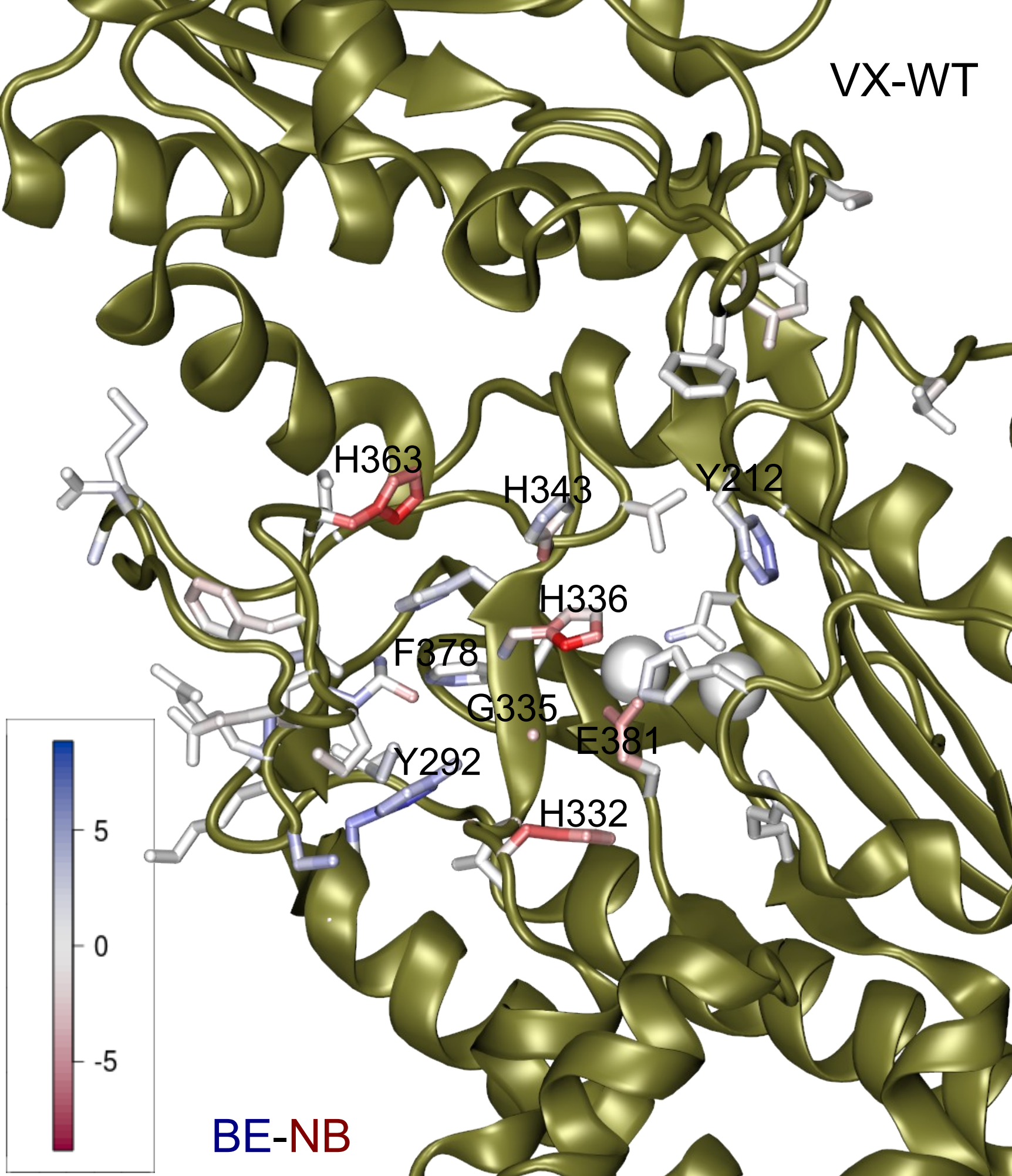
VX-WT
H363
H343
Y212
H336
F378
G335
E381
Y292
H332
5
0
-5
BE-NB

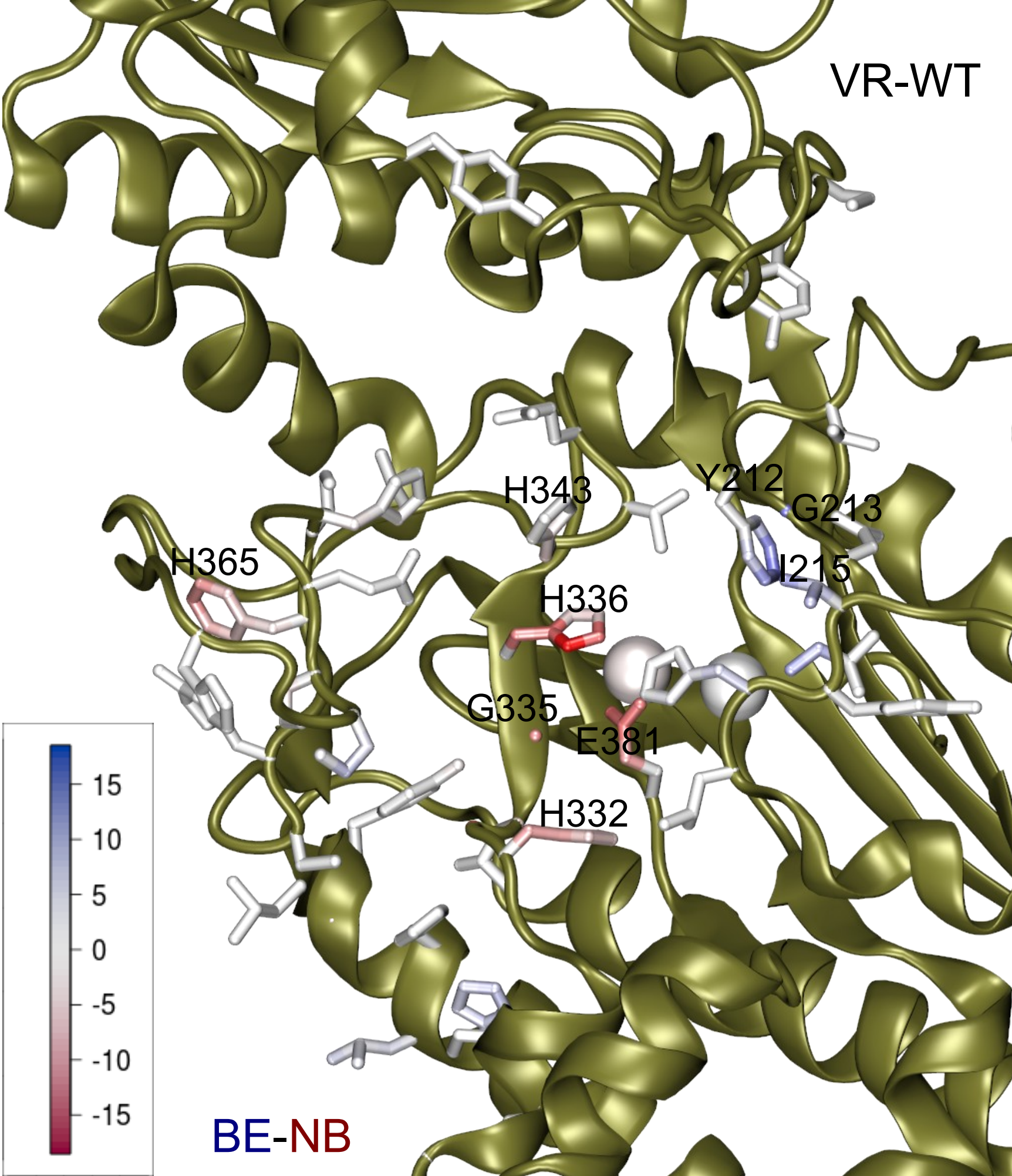
VR-WT
H343
Y212
G213
H365
I215
H336
G335
E381
H332
15
10
5
0
-5
-10
-15
BE-NB

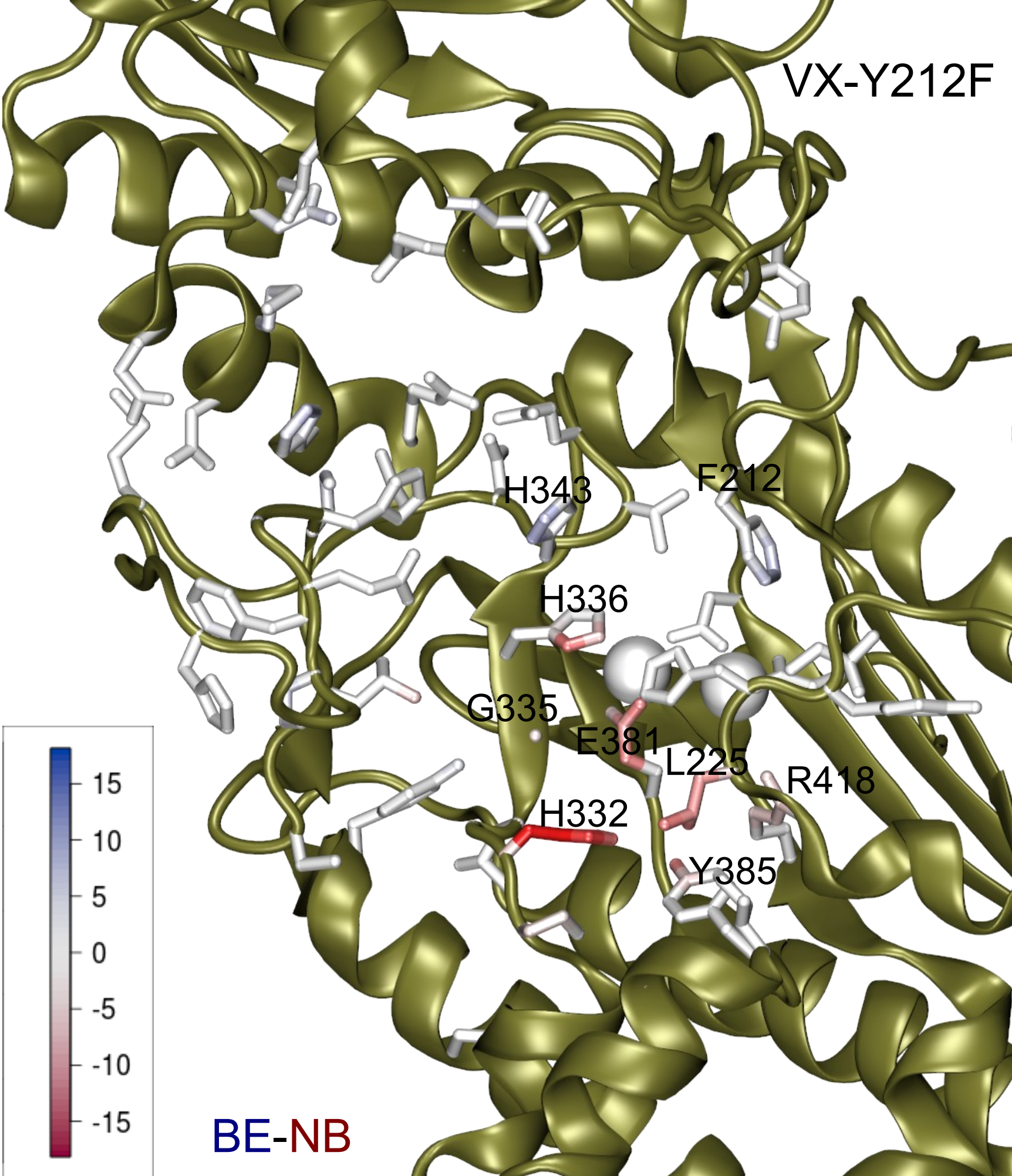
VX-Y212F
H343
F212
H336
G335
E381
L225
R418
H332
Y385
15
10
5
0
-5
-10
-15
BE-NB

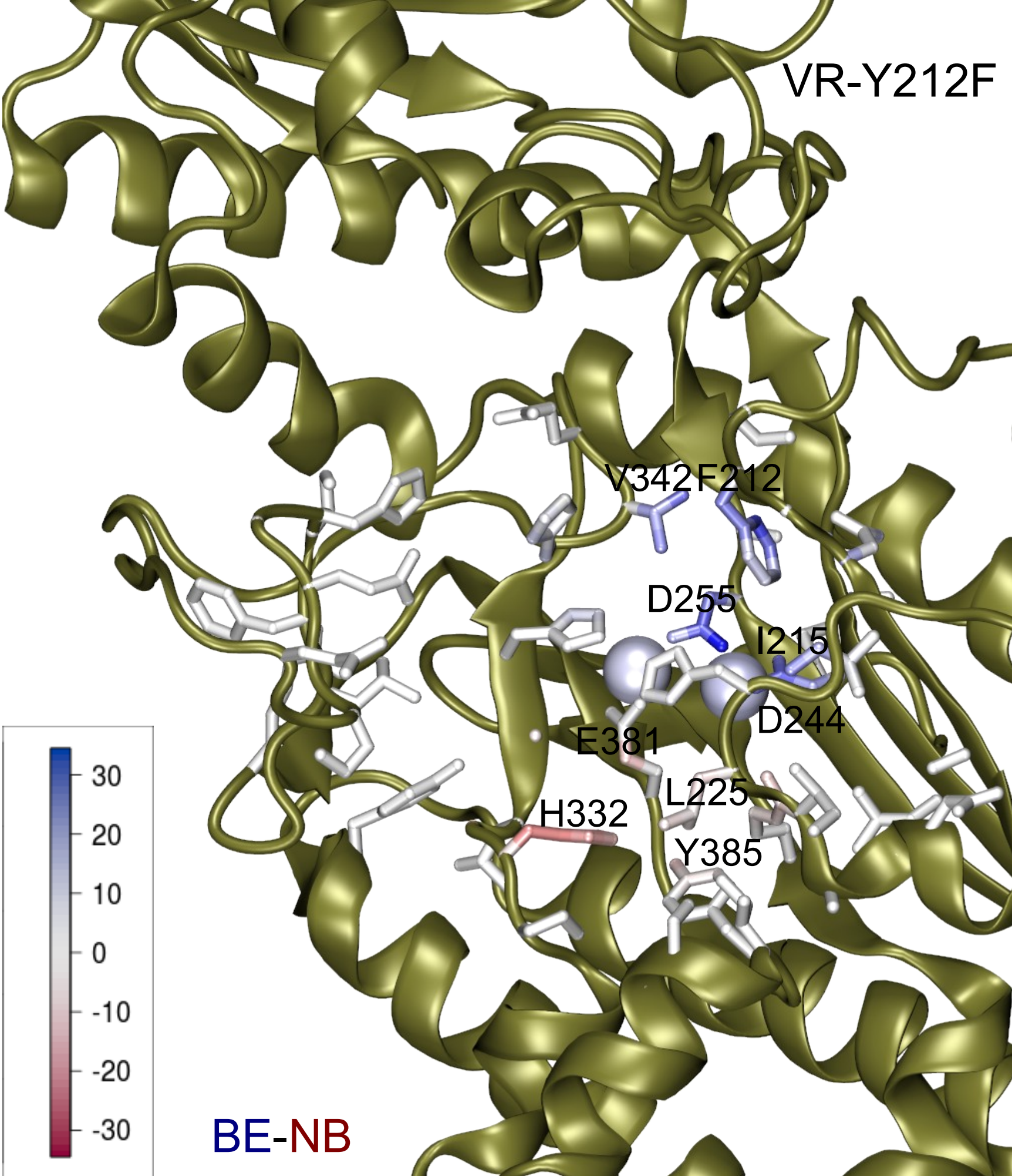
VR-Y212F
V342F212
D255
I215
D244
E381
L225
H332
Y385
30
20
10
0
-10
-20
-30
BE-NB

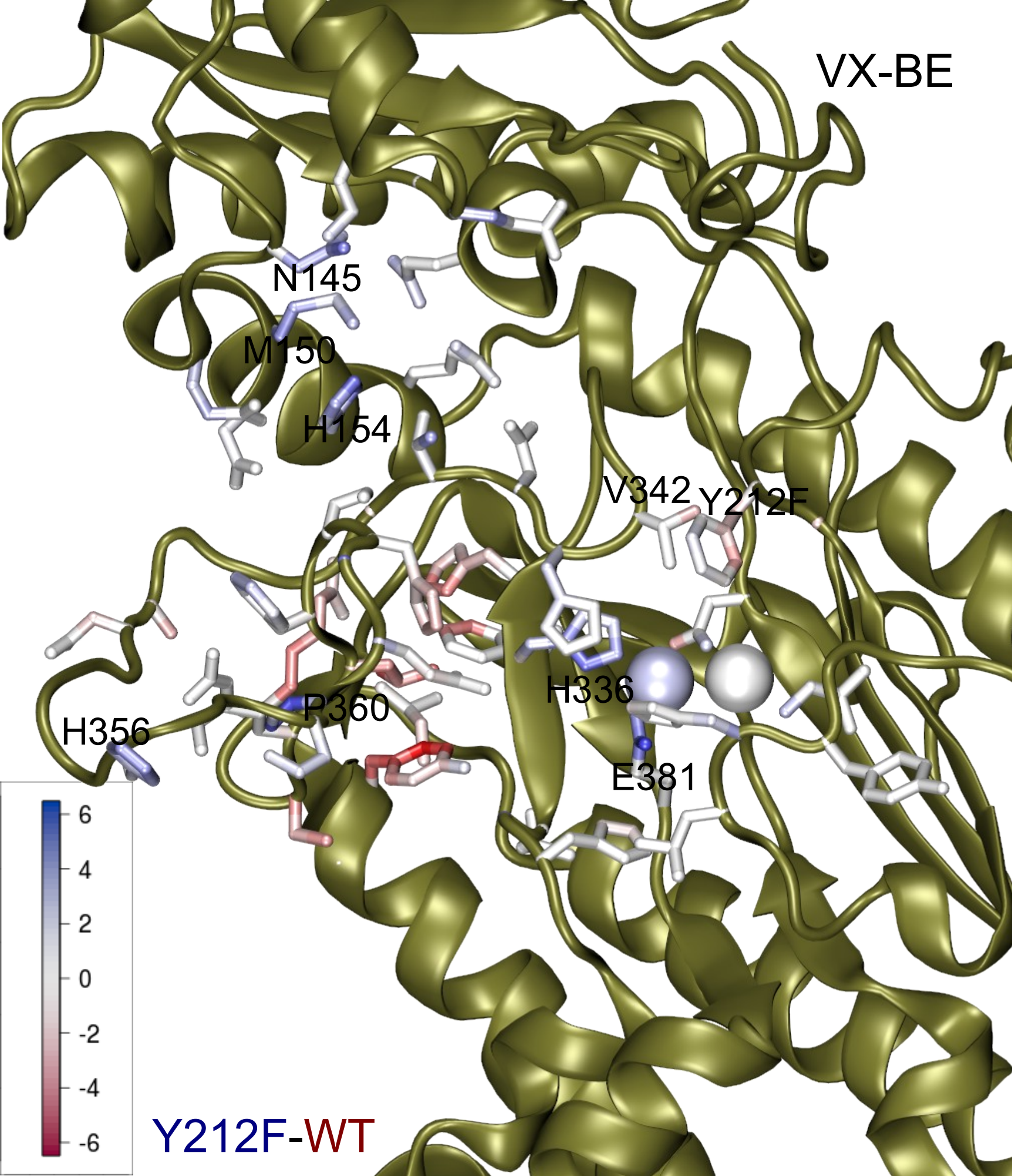
VX-BE
N145
M150
H154
V342
Y212F
H336
P360
H356
E381
6
4
2
0
-2
-4
-6
Y212F-WT

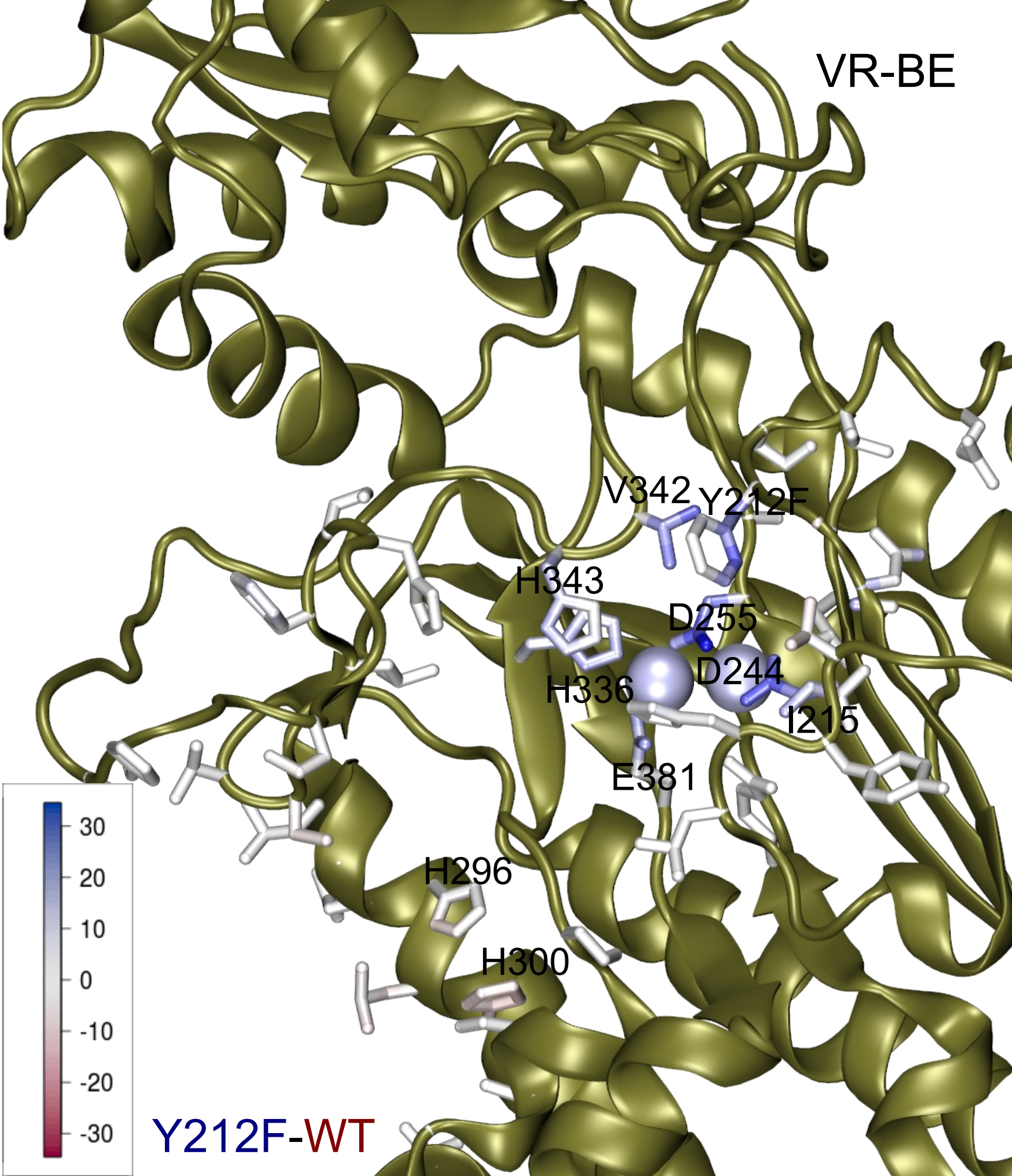
VR-BE
V342
Y212F
H343
D255
D244
H336
I215
E381
H296
H300
30
20
10
0
-10
-20
-30
Y212F-WT

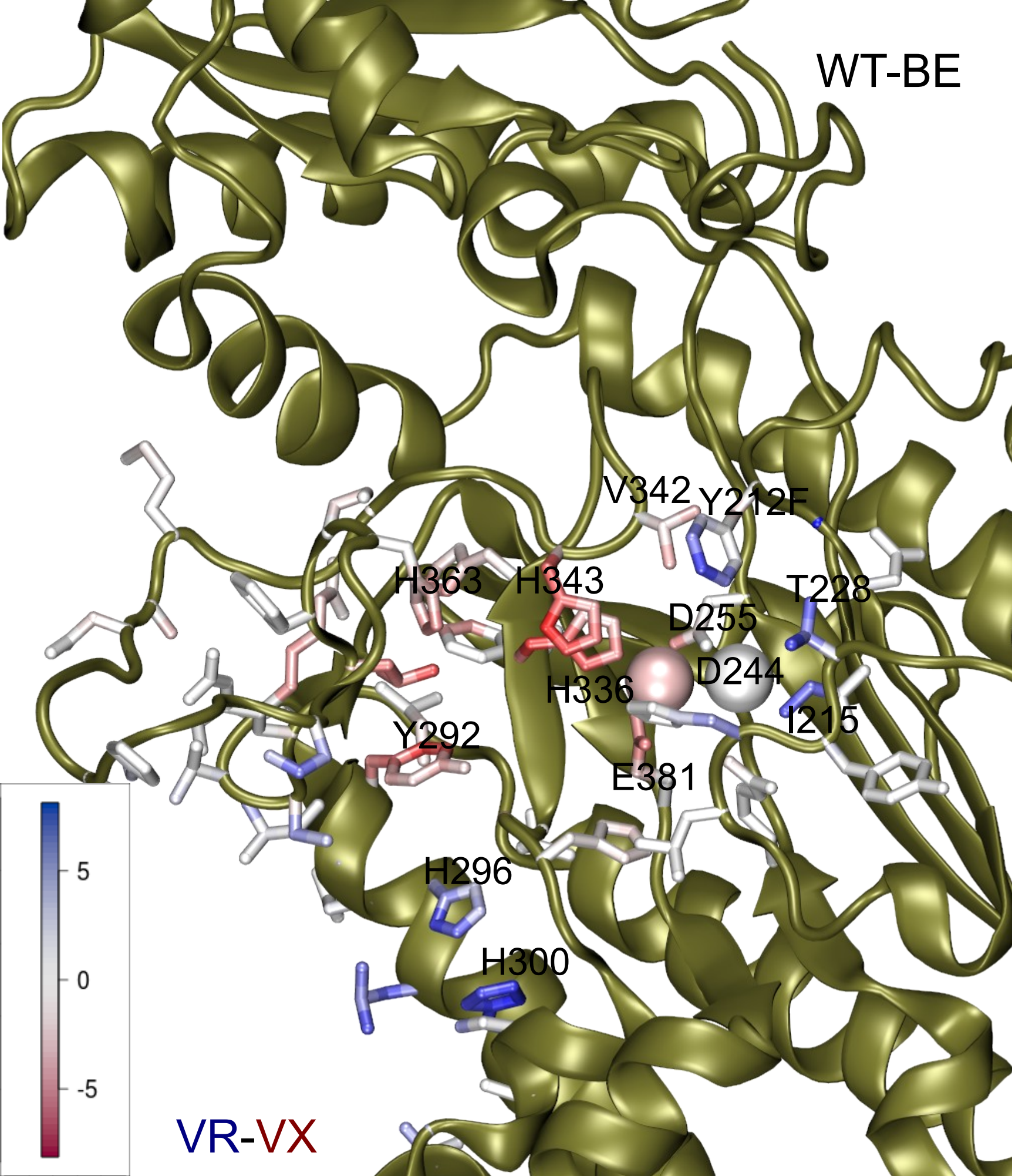
WT-BE
V342
Y212F
H363
H343
T228
D255
D244
H336
I215
Y292
E381
H296
H300
5
0
-5
VR-VX

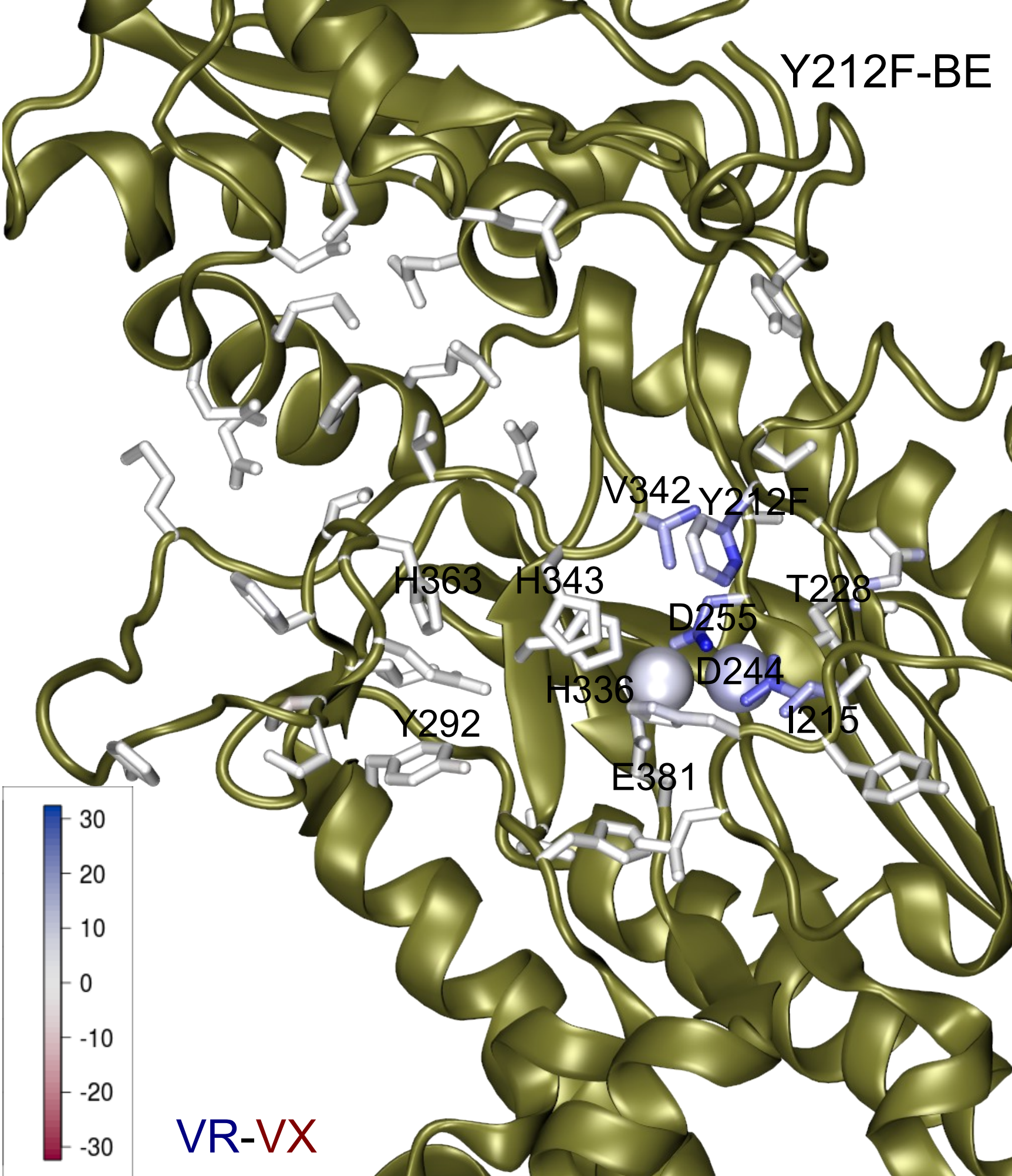
Y212F-BE
V342
Y212F
H363
H343
T228
D255
D244
H336
I215
Y292
E381
30
20
10
0
-10
-20
-30
VR-VX

Supplemental Material

Combined Molecular Simulation and Experimental Engineering of Organophosphorus Acid Anhydrase Yields Enhanced Neutralization of Organophosphorus Nerve Agents

Joshua L. Phillips[1,2], Steven P. Harvey[3], and S. Gnanakaran[1]

[1]Theoretical Biology and Biophysics (T-6) and Center for Nonlinear Studies
Los Alamos National Laboratory, Los Alamos, NM 87545
[2]Department of Computer Science, Middle Tennessee State University, Murfreesboro, TN 37132
[3]US Army Edgewood Chemical Biological Center, Aberdeen, MD 21010

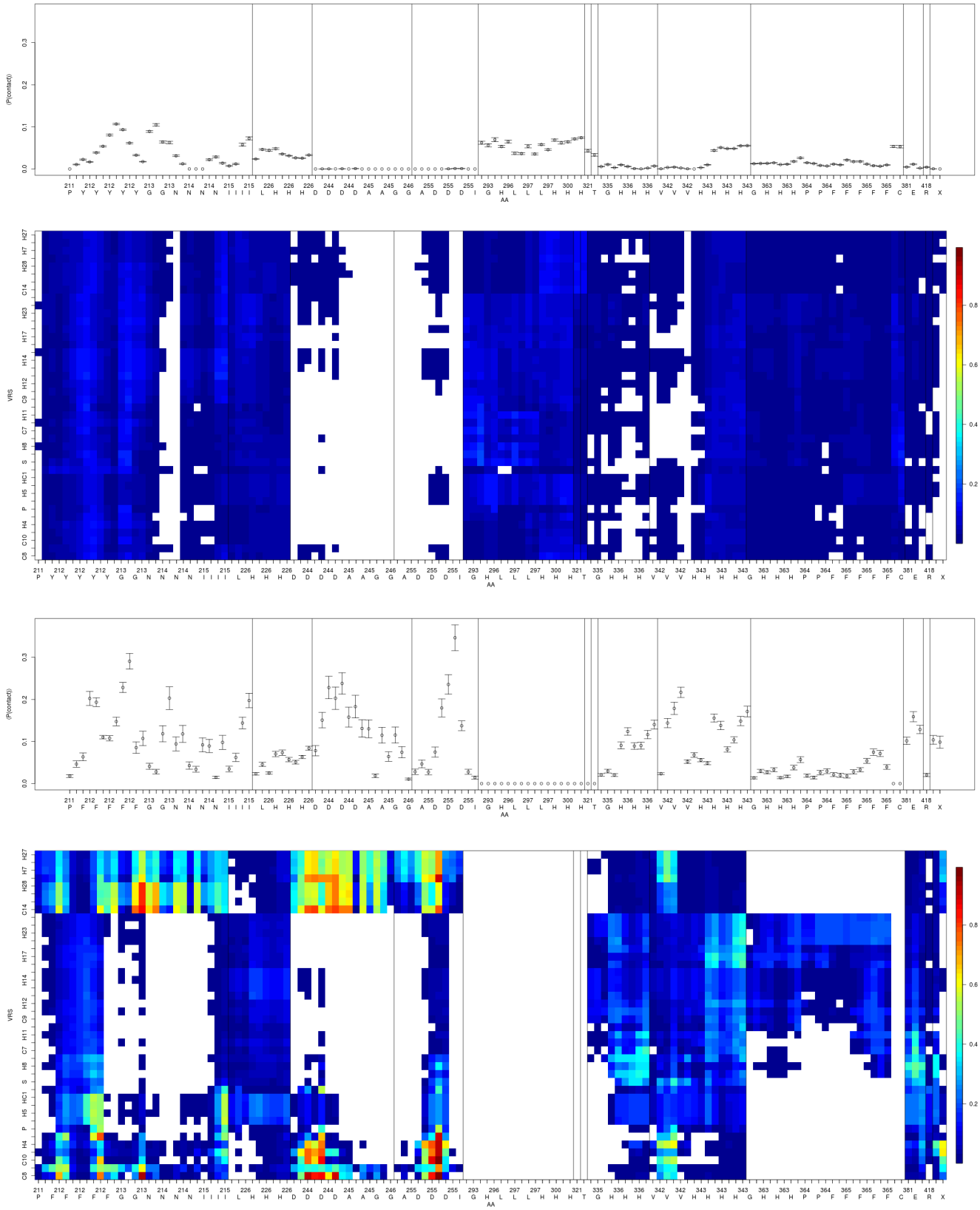

Supplemental Figure 1 – Bonded+Electrostatics model contact profiles showing VR interactions with WT OPAA (top) and the Y212F mutant (bottom).

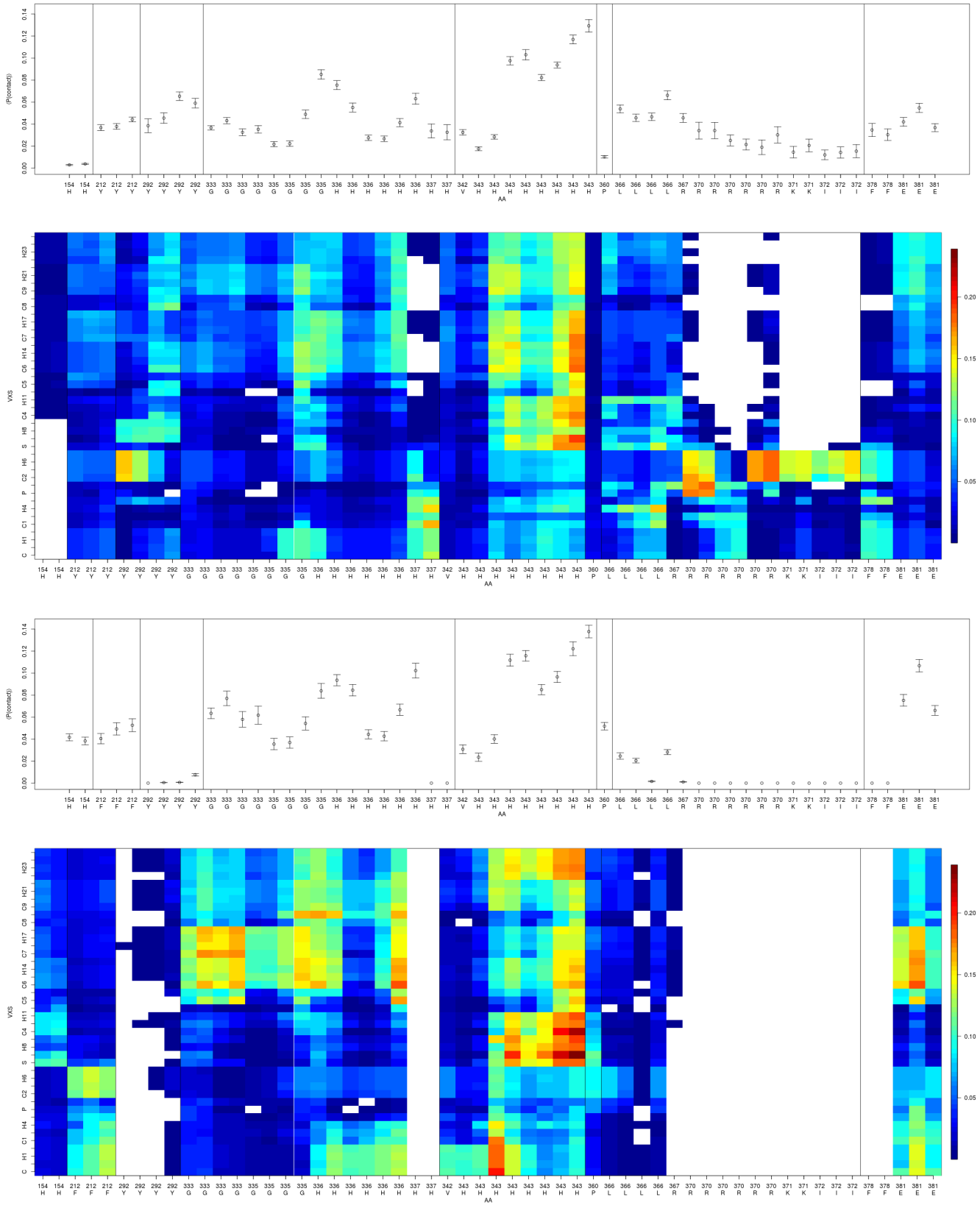

Supplemental Figure 2 – Bonded+Electrostatics model contact profiles showing VX interactions with WT OPAA (top) and the Y212F mutant (bottom).

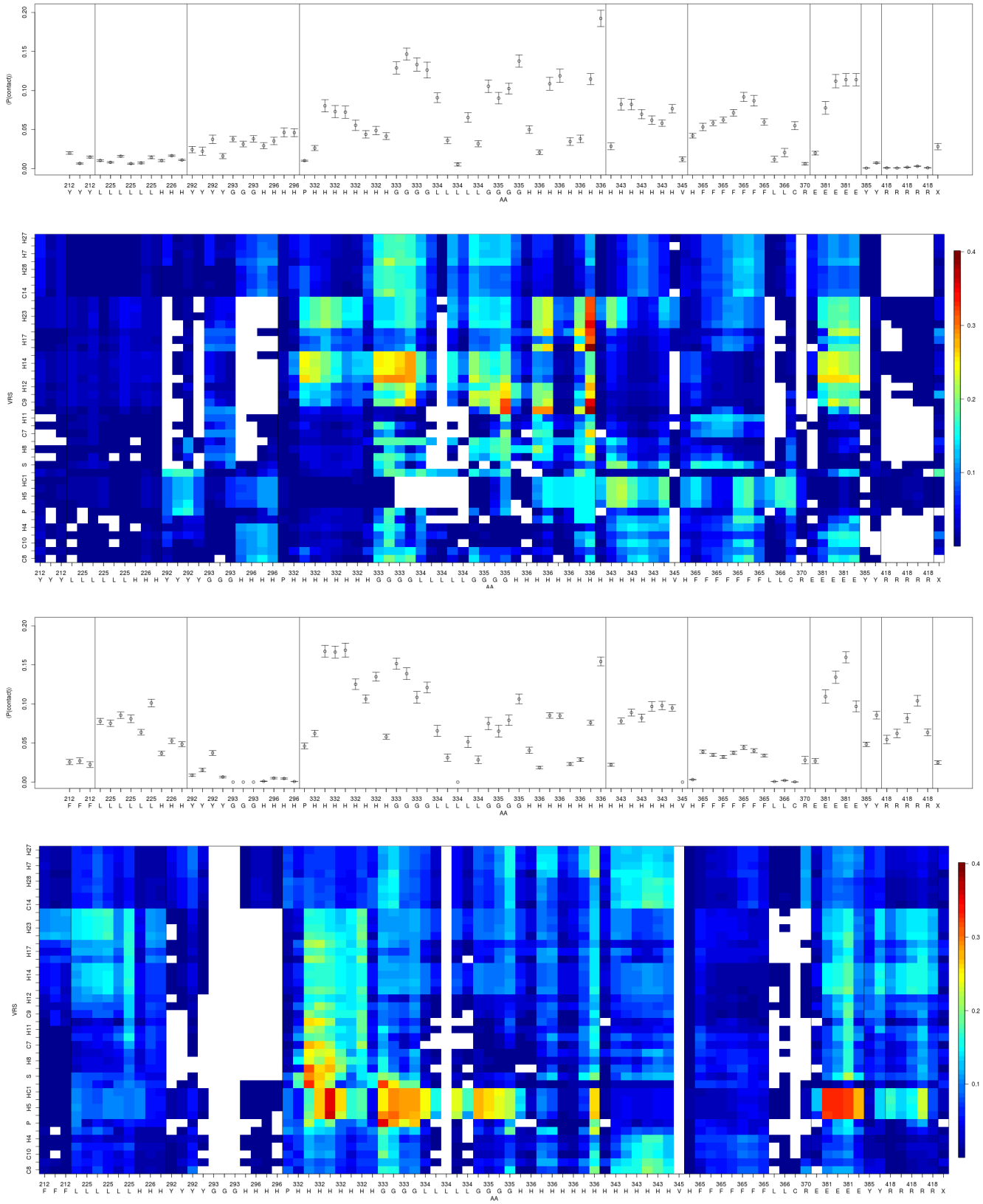

Supplemental Figure 3 – Non-bonded model contact profiles showing VR interactions with WT OPAA (top) and the Y212F mutant (bottom).

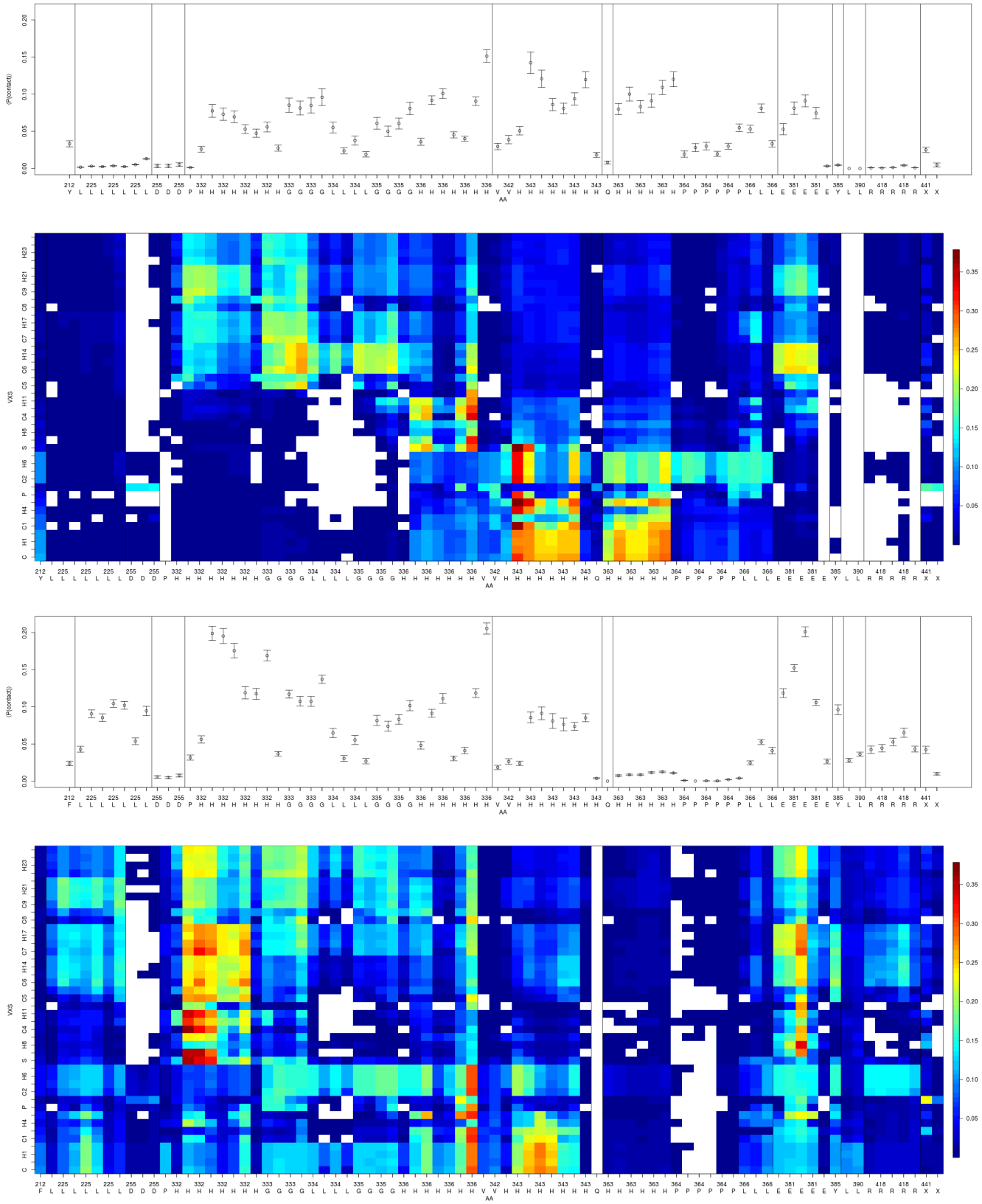

Supplemental Figure 4 – Non-bonded model contact profiles showing VX interactions with WT OPAA (top) and the Y212F mutant (bottom).

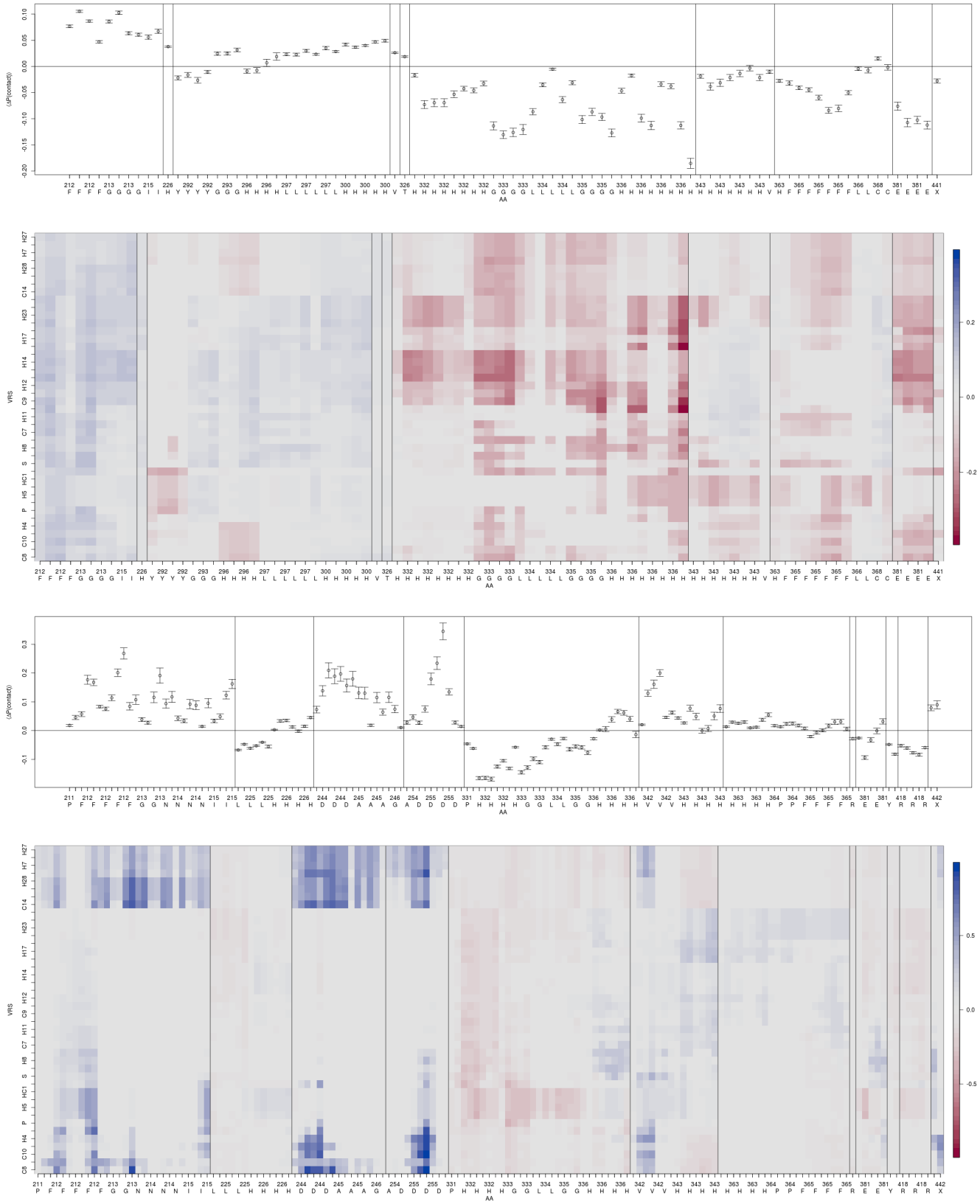

Supplemental Figure 5 – Differences between contact profiles for the bonded+electrostatics and non-bonded models showing VR interactions with WT OPAA (top) and the Y212F mutant (bottom).

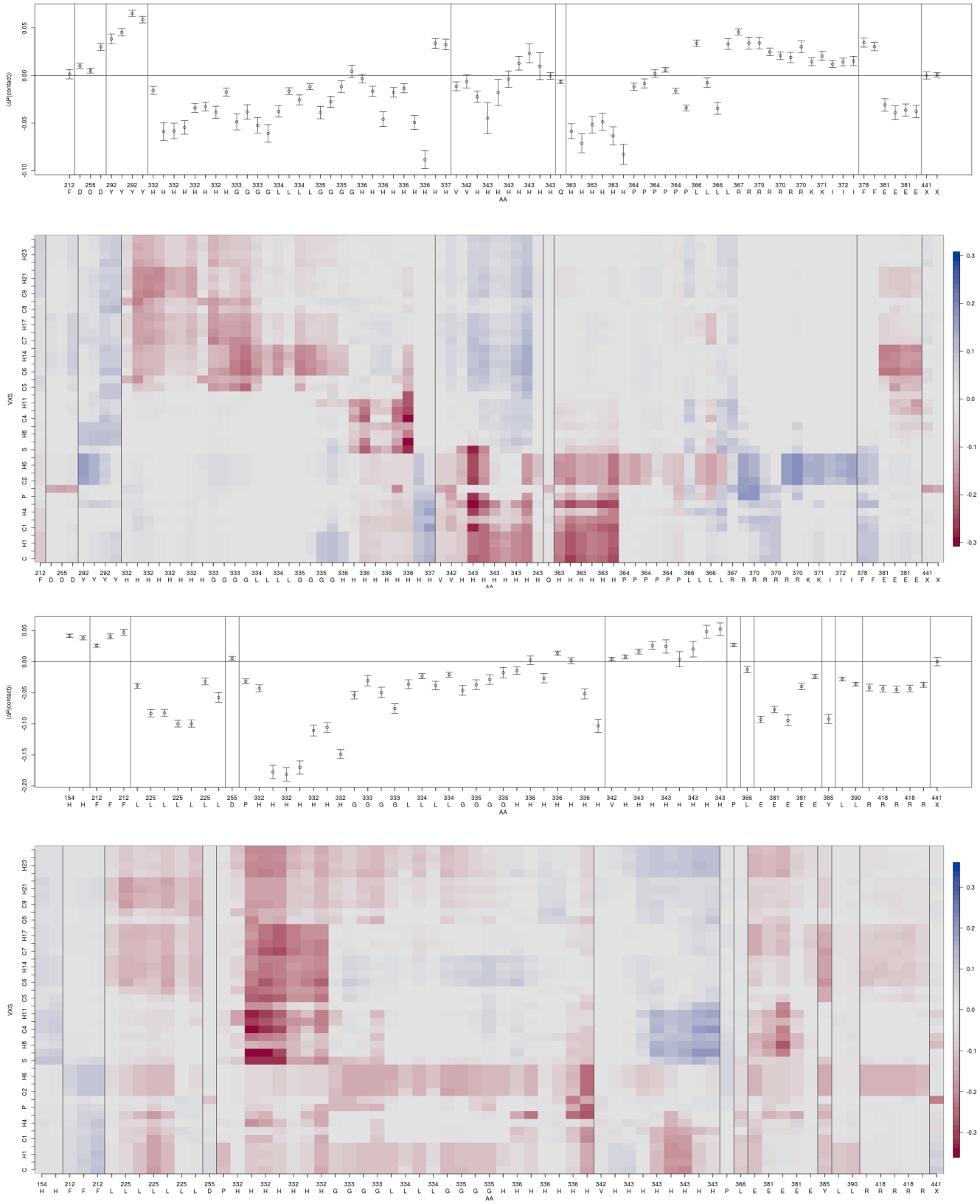

Supplemental Figure 6 – Differences between contact profiles for the bonded+electrostatics and non-bonded models showing VX interactions with WT OPAA (top) and the Y212F mutant (bottom).

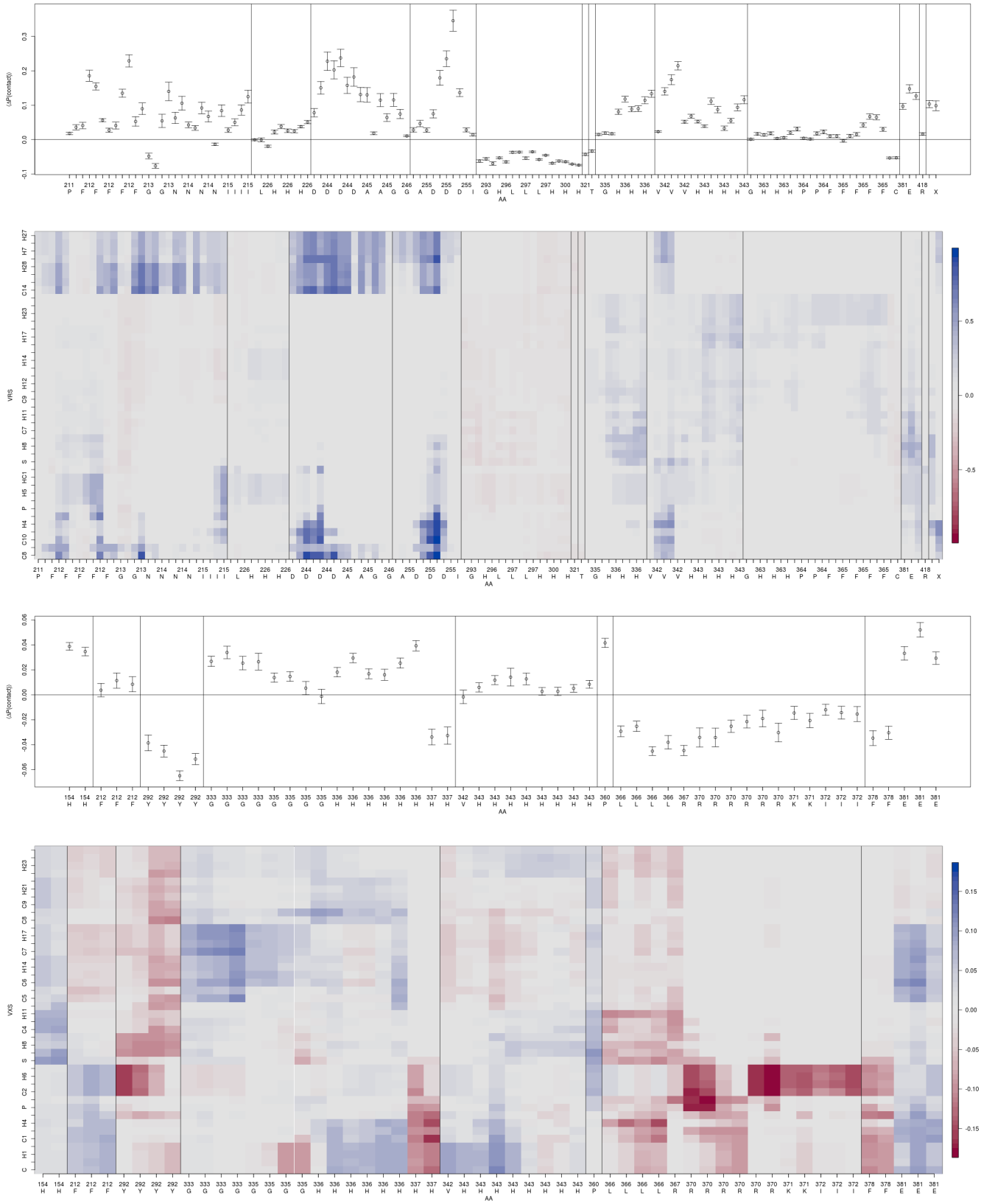

Supplemental Figure 7 – Differences between the contact profiles for the bonded+electrostatics models for WT OPAA and the Y212F mutant with interactions between VR (top) and VX (bottom).

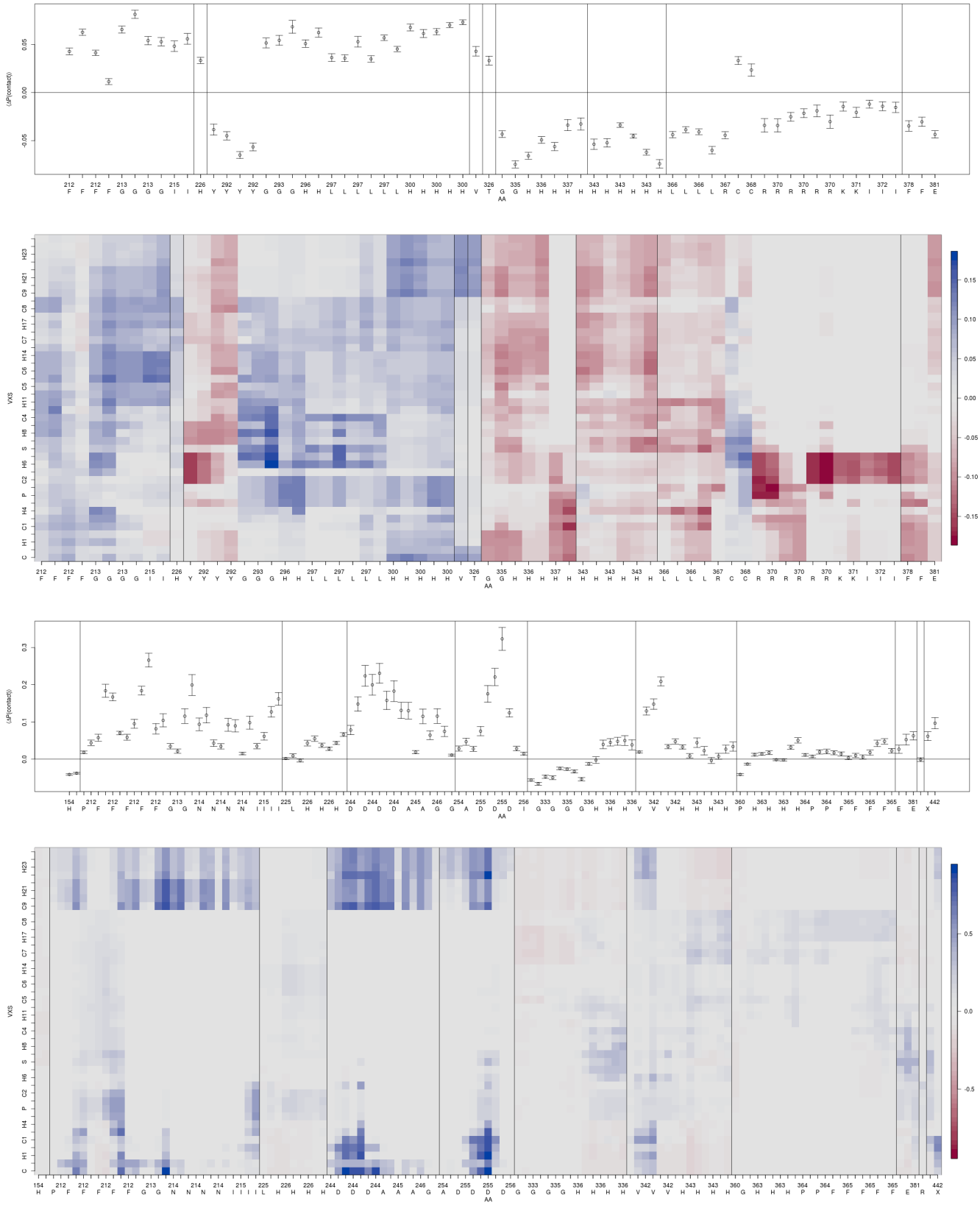

Supplemental Figure 8 – Differences between the contact profiles for the bonded+electrostatics models for VR and VX interacting with WT OPAA (top) and the Y212F mutant (bottom).

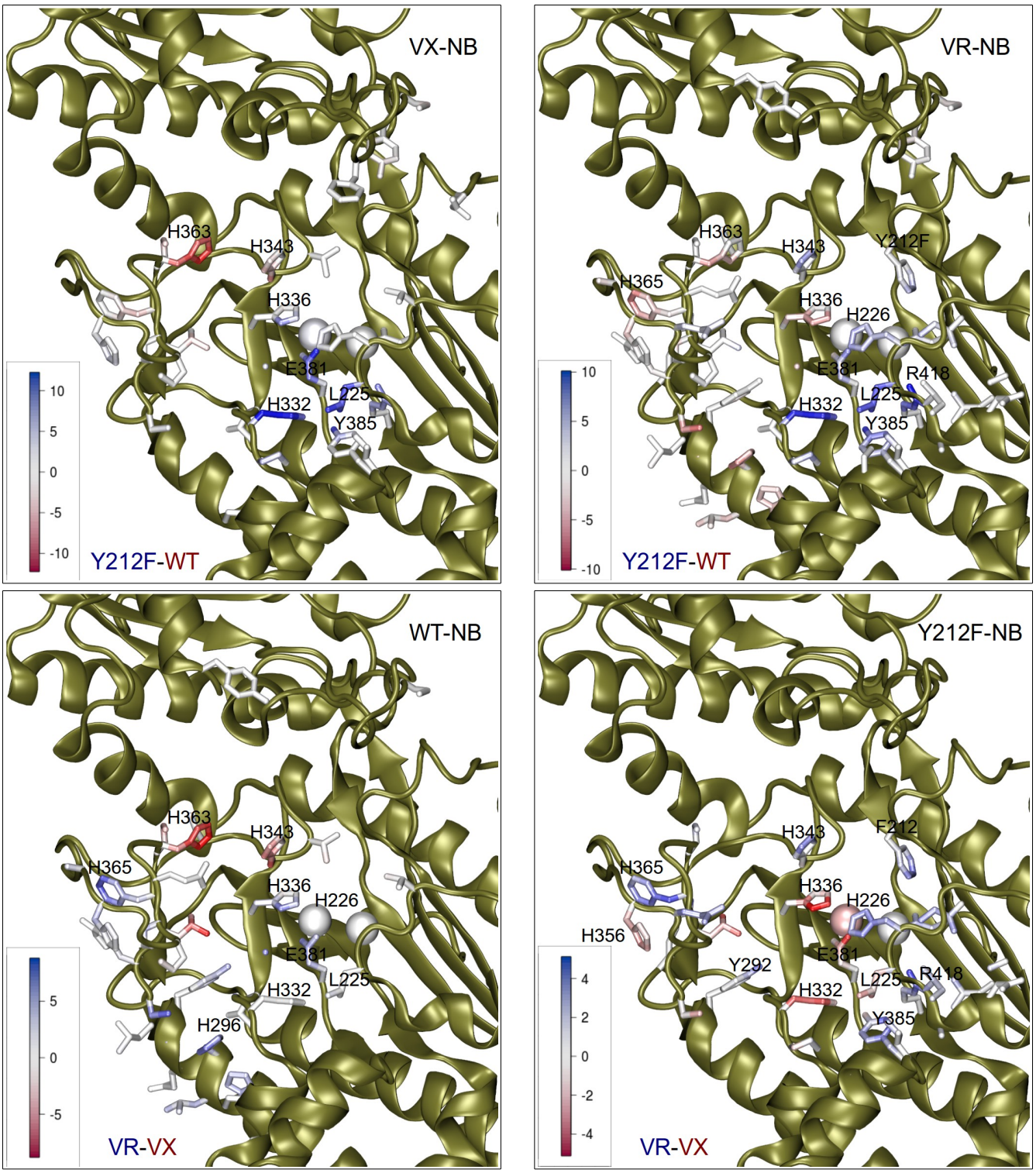

Supplemental Figure 9 – Differences between the contact profiles for the non-bonded models for VX (top-left) and VR (top-right) interacting with OPAA, WT OPAA (bottom-left), and the Y212F mutant (bottom-right).

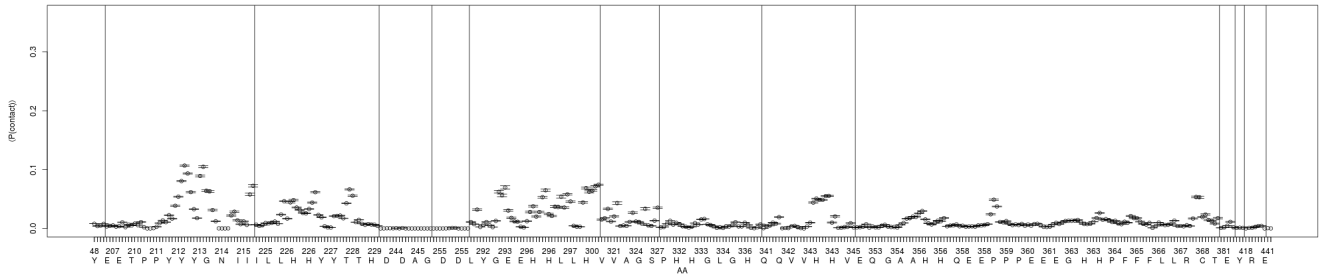

VR-WT-BE

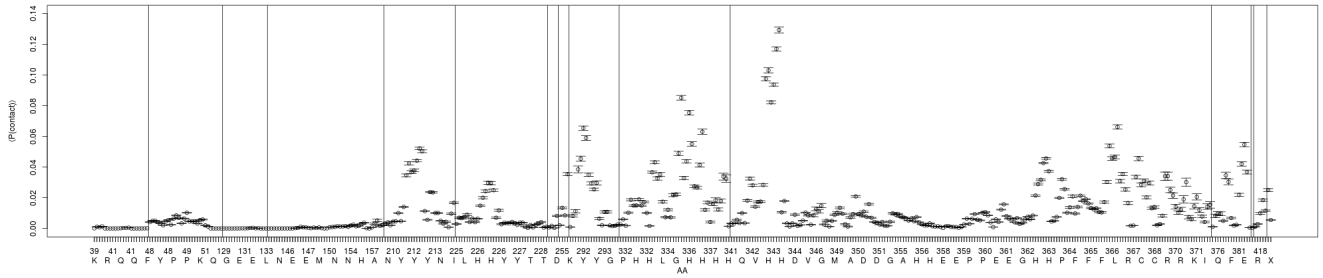

VX-WT-BE

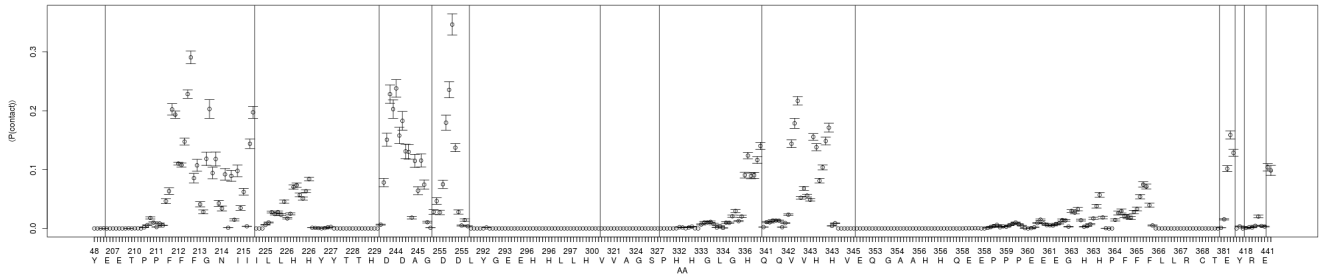

VR-Y212F-BE

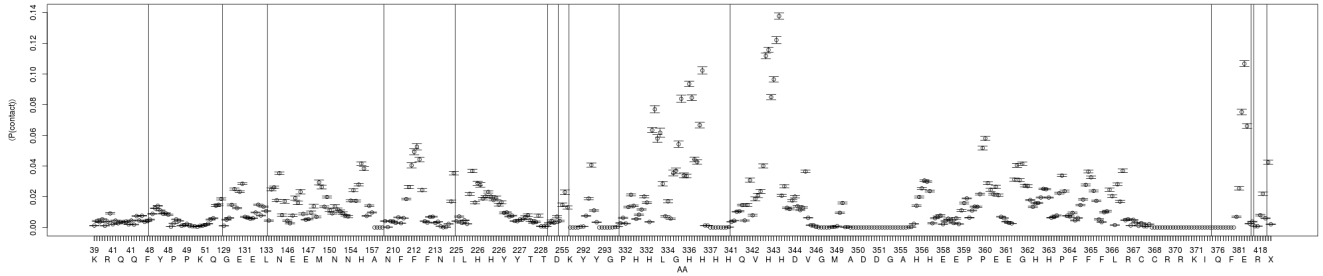

VX-Y212F-BE

Supplemental Figure 10 – Small cutoff (P_{cutoff}=0.01) contact profiles for the bonded+electrostatics models.

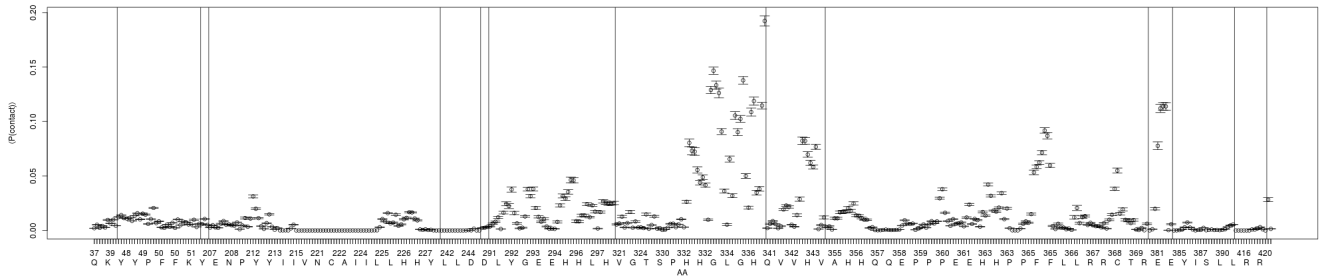

VR-WT-NB

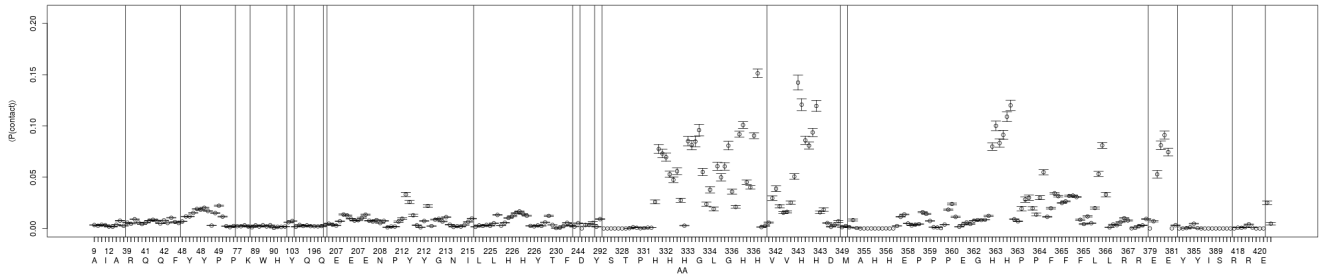

VX-WT-NB

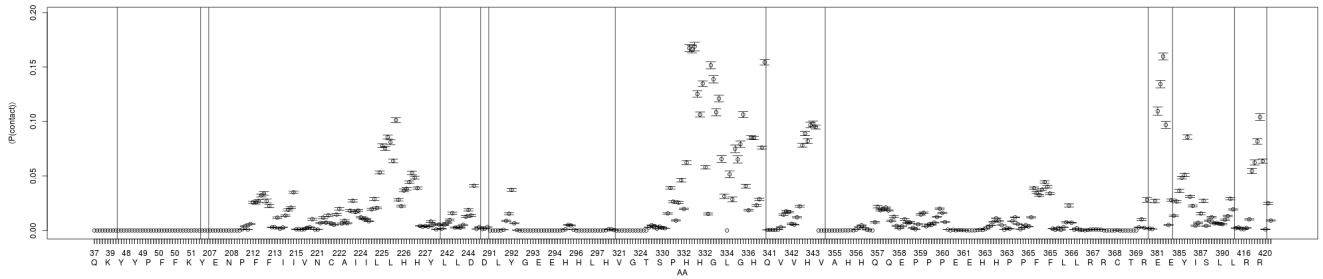

VR-Y212F-NB

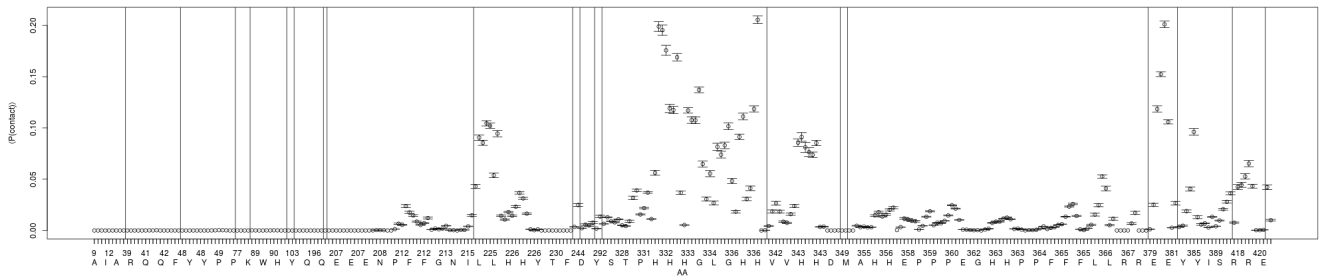

VX-Y212F-NB

Supplemental Figure 11 – Small cutoff (P_{cutoff}=0.01) contact profiles for the non-bonded models.

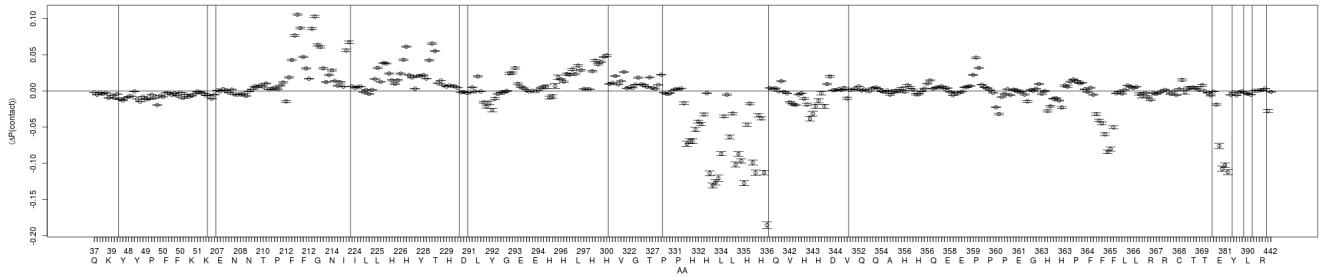

VR-WT-(BE-NB)

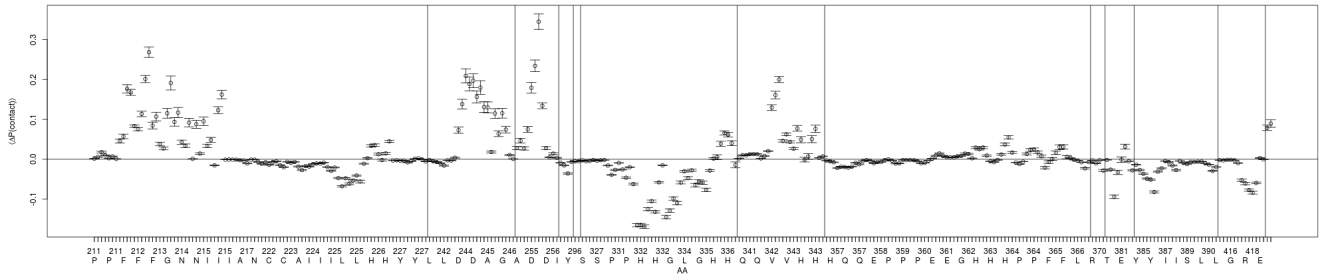

VR-Y212F-(BE-NB)

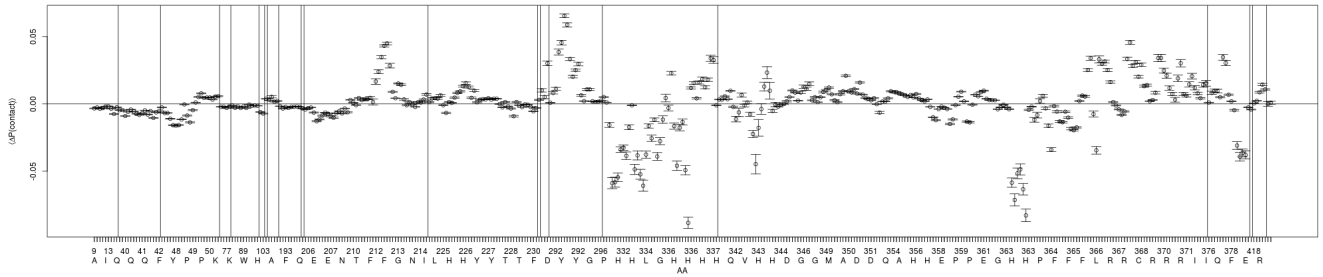

VX-WT-(BE-NB)

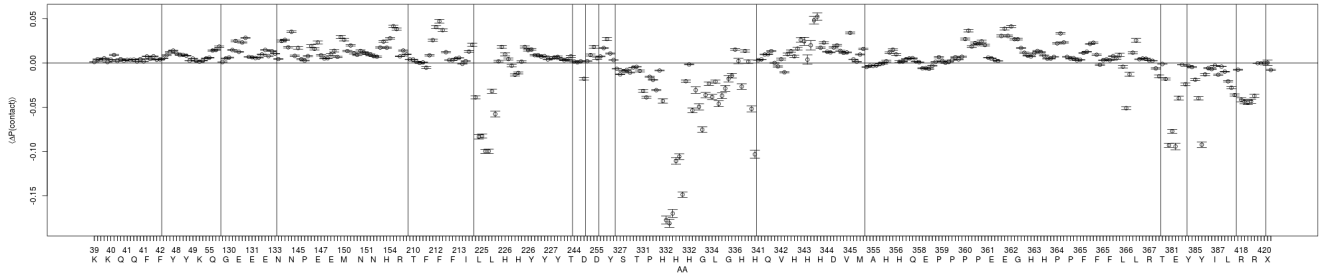

VX-Y212F-(BE-NB)

Supplemental Figure 12 – Small cutoff (P_{cutoff}=0.01) contact profile differences between the BE and NB models.

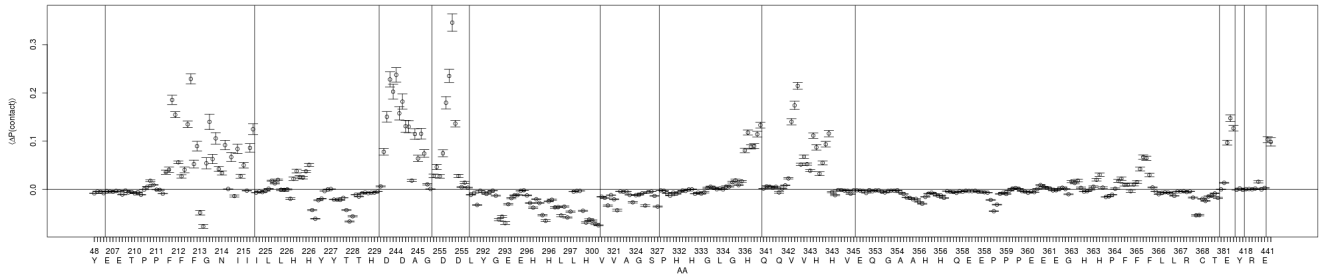

VR-(Y212F-WT)-BE

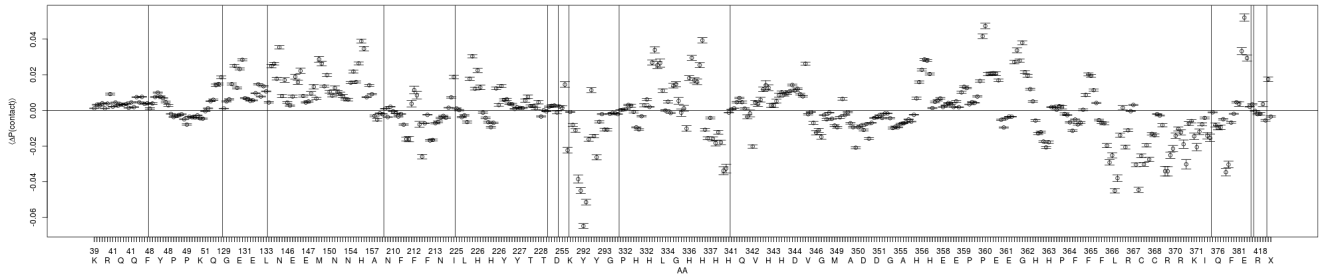

VX-(Y212F-WT)-BE

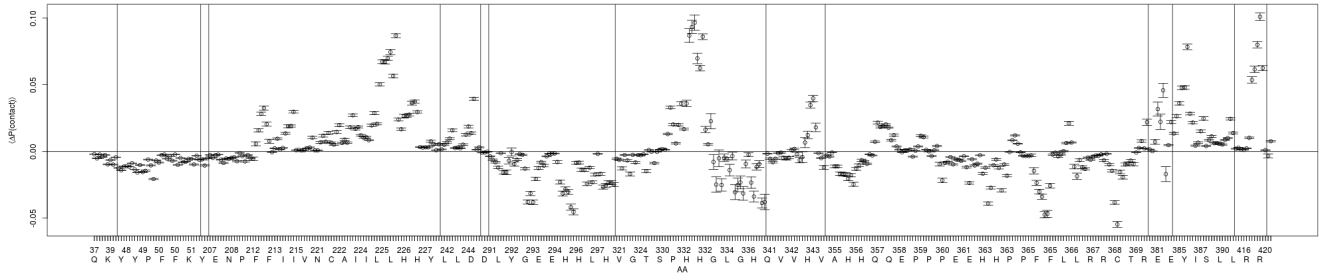

VR-(Y212F-WT)-NB

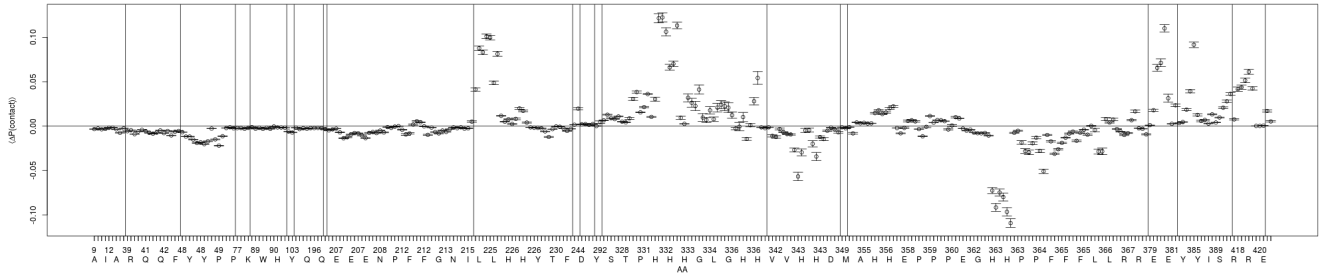

VX-(Y212F-WT)-NB

Supplemental Figure 13 – Small cutoff (P_{cutoff}=0.01) contact profile differences for WT OPAA and the Y212F mutant.

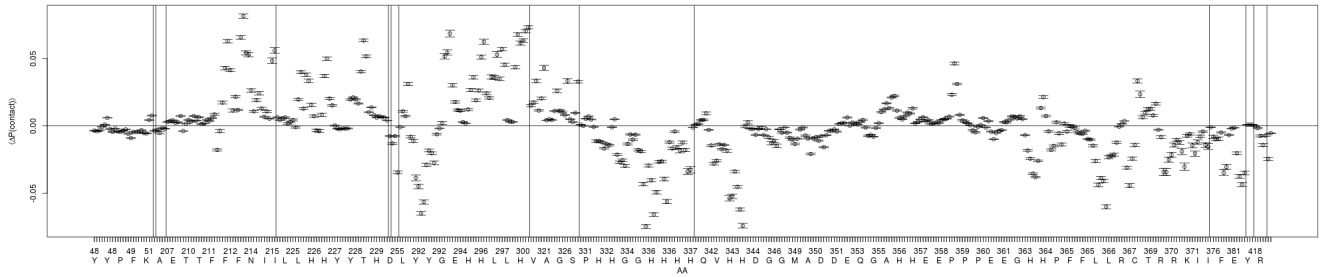

(VR-VX)-WT-BE

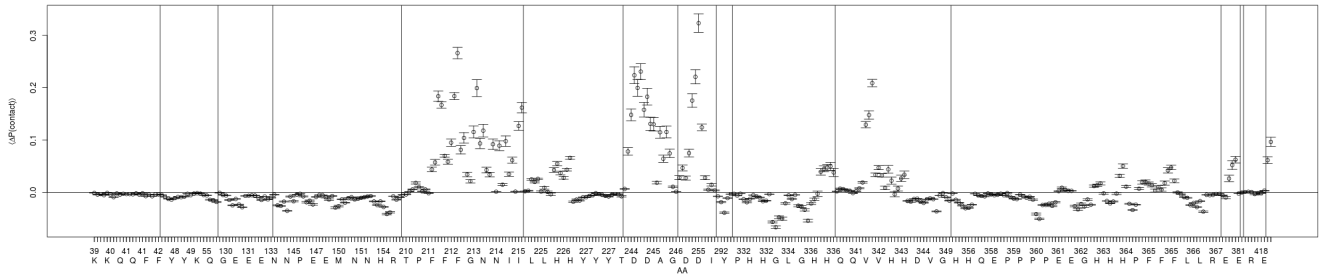

(VR-VX)-Y212F-BE

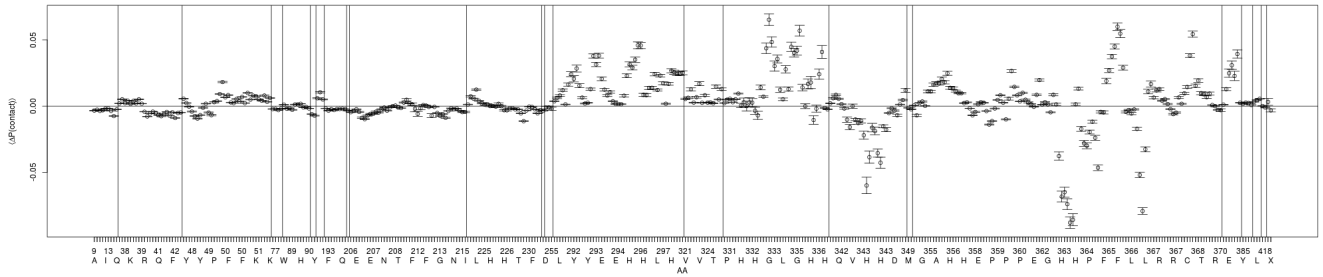

(VR-VX)-WT-NB

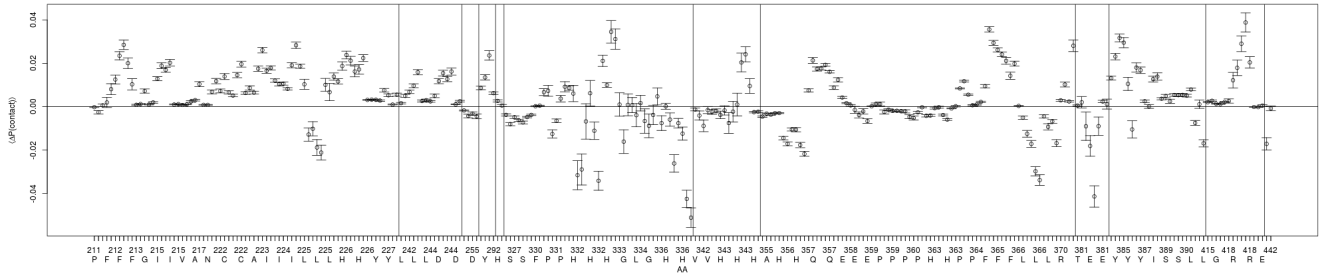

(VR-VX)-Y212F-NB

Supplemental Figure 14 – Small cutoff (P_{cutoff}=0.01) contact profile differences for VR and VX.